

# ASTRODEEP-JWST: NIRCам-HST multiband photometry and redshifts for half a million sources in six extragalactic deep fields

E. Merlin<sup>1</sup>, P. Santini<sup>1</sup>, D. Paris<sup>1</sup>, M. Castellano<sup>1</sup>, A. Fontana<sup>1</sup>, T. Treu<sup>2</sup>, S. L. Finkelstein<sup>3</sup>, J. S. Dunlop<sup>4</sup>, P. Arrabal Haro<sup>5</sup>, M. Bagley<sup>3</sup>, K. Boyett<sup>6,7</sup>, A. Calabrò<sup>1</sup>, M. Correnti<sup>1,8</sup>, K. Davis<sup>9</sup>, M. Dickinson<sup>5</sup>, C. T. Donnan<sup>4</sup>, H. C. Ferguson<sup>10</sup>, F. Fortuni<sup>1</sup>, M. Giavalisco<sup>11</sup>, K. Glazebrook<sup>12</sup>, A. Grazian<sup>13</sup>, N. A. Grogin<sup>10</sup>, N. Hathi<sup>10</sup>, M. Hirschmann<sup>14</sup>, J. S. Kartaltepe<sup>15</sup>, L. J. Kewley<sup>16</sup>, A. Kirkpatrick<sup>17</sup>, D. D. Kocevski<sup>18</sup>, A. M. Koekemoer<sup>10</sup>, G. Leung<sup>3</sup>, J. M. Lotz<sup>10</sup>, D. K. Magee<sup>19</sup>, D. Marchesini<sup>20</sup>, S. Mascia<sup>1</sup>, D. J. McLeod<sup>4</sup>, R. J. McLure<sup>4</sup>, T. Nanayakkara<sup>12</sup>, L. Napolitano<sup>1,21</sup>, M. Nonino<sup>22</sup>, C. Papovich<sup>23,24</sup>, L. Pentericci<sup>1</sup>, P. G. Pérez-González<sup>25</sup>, N. Pirzkal<sup>26</sup>, S. Ravindranath<sup>27,28</sup>, G. Roberts-Borsani<sup>29</sup>, R. S. Somerville<sup>30</sup>, M. Trenti<sup>6,7</sup>, J. R. Trump<sup>9</sup>, B. Vulcani<sup>13</sup>, X. Wang<sup>31,32,33</sup>, P. J. Watson<sup>13</sup>, S. M. Wilkins<sup>34,35</sup>, G. Yang<sup>36,37</sup>, and L. Y. A. Yung<sup>10</sup>

(Affiliations can be found after the references)

Received XXX; accepted XXX

## ABSTRACT

**Aims.** We present a set of photometric catalogs primarily aimed at providing the community with a comprehensive database for the study of galaxy populations in the high redshift Universe. The set gathers data from eight *JWST* NIRCам observational programs, targeting the Abell 2744 (GLASS-JWST, UNCOVER, DDT2756 and GO3990), EGS (CEERS), COSMOS and UDS (PRIMER), and GOODS North and South (JADES and NGDEEP) deep fields, for a total area of  $\approx 0.2$  sq. degrees.

**Methods.** Photometric estimates are obtained by means of well-established techniques, including tailored improvements designed to enhance the performance on the specific dataset. We also include new measurements from *HST* archival data, thus collecting 16 bands spanning from 0.44 to 4.44  $\mu\text{m}$ .

**Results.** A grand total of  $\sim 530$  thousand sources is detected on stacks of NIRCам 3.56 and 4.44  $\mu\text{m}$  mosaics. We assess the photometric accuracy by comparing fluxes and colors against archival catalogs. We also provide photometric redshift estimates, statistically validated against a large set of robust spectroscopic data.

**Conclusions.** The catalogs are publicly available on the ASTRODEEP website.

**Key words.** galaxies: high redshift, galaxies: photometry

## 1. Introduction

Two years since its first light, the James Webb Space Telescope (*JWST*, Gardner et al. 2006, 2023) has provided many cutting-edge quality data to many fields of astrophysical research. In particular, the study of the high redshift Universe has benefited from the joint effort of researchers designing tailored observational programs and exploiting their outcomes, with an outburst of activity within the very first weeks after the arrival of the first data (see e.g. Adamo et al. 2024, for a review).

The unmatched depth and resolution of *JWST* infrared imaging and spectroscopy has enabled a wealth of analysis at intermediate and high redshifts that were beyond reach of previous instruments, from the measurement of optical rest-frame morphologies (e.g., Jacobs et al. 2023; Treu et al. 2023; Kartaltepe et al. 2023), stellar masses (e.g., Santini et al. 2023; Weibel et al. 2024; Wang et al. 2024) and star-formation histories (e.g., Dressler et al. 2023; Looser et al. 2023; Ciesla et al. 2023) of galaxies up to  $z \approx 10$ , to the abundance and properties of red and optically-dark sources (e.g., Glazebrook et al. 2023; Kirkpatrick et al. 2023; Pérez-González et al. 2023a; Rodighiero et al. 2024) and quiescent galaxies (e.g., Carnall et al. 2023; Nanayakkara et al. 2024; Wright et al. 2024; Ward et al. 2024) up to  $z \sim 6$ , the properties of compact red sources (Pérez-González et al. 2024; Williams et al. 2024; Kokorev et al. 2024), or the identification

of extreme emission line galaxies in the reionization epoch (e.g. Davis et al. 2023). In particular, *JWST* has challenged our view of the early epochs of the cosmos. A number of exciting discoveries on the first phases of galaxy formation and evolution have resulted in more questions than answers, as we have yet to frame and understand our observations within a fully consistent theoretical framework. The most consolidated result so far is the evidence of a striking overabundance of bright galaxies at  $z \gtrsim 9-10$  compared to most predictions (e.g., Castellano et al. 2022, 2023; Naidu et al. 2022; Finkelstein et al. 2023a,b; McLeod et al. 2024; Pérez-González et al. 2023b; Carniani et al. 2024). These distant sources have been mostly identified by means of color selections or spectral energy distribution (SED) fitting, and the result is still a matter of debate, with many possible explanations proposed (e.g. Ferrara et al. 2023; Dekel et al. 2023; Mason et al. 2023; Trinca et al. 2024; Padmanabhan & Loeb 2023; Yung et al. 2024). While spectroscopic follow-up is crucial to understand the physical processes at play, and indeed they currently seem to confirm the early results (e.g. Arrabal Haro et al. 2023a; Harikane et al. 2024; Castellano et al. 2024), photometric data still constitute the primary way to collect statistically significant samples, beyond providing targets for spectroscopy.

In this paper we present our analysis of eight deep-sky NIRCам observational programs: CEERS, DDT2756, GLASS-JWST, GO3990, JADES, NGDEEP, PRIMER and UNCOVER,

from which we created a new set of photometric catalogs, mainly finalized to provide a consistent database for the study of the early phases of galaxy evolution in the high redshift Universe ( $z \geq 3$ ). The programs target six among the most well-known and studied areas of the sky, already observed with *HST* and ground-based facilities (in particular, the CANDELS and Frontier Fields campaigns, see Grogin et al. 2011; Koekemoer et al. 2011; Lotz et al. 2014), and subject of many ground-breaking studies in the past decades: (i) the GLASS-JWST, UNCOVER, DDT2756 and GO3990 programs cover the Abell 2744 cluster of galaxies, also known as Pandora’s cluster, and its surrounding area. For simplicity, we will refer to this extended region as ABELL2744; (ii) the CEERS survey overlaps with the Extended Groth Strip (EGS) field (Davis et al. 2007); (iii-iv) the PRIMER program covers two areas, one overlapping with the UKIDSS Ultra-deep Survey field (UDS, Lawrence et al. 2007) and the other with the COSMOS field (Nayyeri et al. 2017); (vi) JADES and NGDEEP overlap with the GOODS-North and ECDFS/GOODS-South regions (Giacconi et al. 2002; Giavalisco et al. 2004). The total area observed by these programs is  $\approx 0.2$  sq. degrees. While some catalogs for these observations are already available (e.g. Paris et al. 2023; Rieke et al. 2023; Weaver et al. 2024), the aim of this new dataset is to provide a large, self-consistent database mainly aimed at the study of the high redshift Universe. Therefore, we mostly focused our attention on the detection of faint sources when choosing detection parameters. Unsurprisingly, this choice can lead to some degree of tension when comparing our results to other catalogs (see Sect. 4).

The new catalogs are obtained with well-tested algorithms and techniques, largely building upon previous releases of our group (Merlin et al. 2022; Paris et al. 2023, respectively M22 and P23 hereafter), but with substantial improvements, that we describe in Section 3. Up-to-date data and calibration files have been used whenever available (detailed information is provided). We also estimated photometric redshift, which we obtained using the *zPHOT* SED-fitting software, first described in Fontana et al. (2000), and EAZY (Brammer et al. 2008) exploiting three different sets of templates. Predictably, we find that while for high signal-to-noise (SNR) the four runs typically yield estimates in reasonable agreement, faint objects are less well constrained, often resulting in divergent fits. Finally, we validate our results comparing them to the literature. We find substantial agreement with other photometric catalogs, and good statistics checking the photo- $z$ ’s against spectroscopic data.

The paper is organized as follows. In Sect. 2 we describe the dataset. In Sect. 3 we summarise the adopted techniques, referencing previous publications when useful, and highlighting the differences with previous works. In Sect. 4 we discuss the validation of our new catalogs against published data, considering direct comparisons of colors. In Sect. 5 we discuss photometric redshifts. In Sect. 6 we make some final remarks and conclusions. The catalog format is described in Appendix A. We use AB magnitudes (Oke & Gunn 1983) and we assume a  $\Lambda$ CDM cosmology ( $H_0 = 70$  km/s/Mpc,  $\Omega_m = 0.27$  and  $\Omega_\Lambda = 0.73$ ). The catalogs are publicly available on the ASTRODEEP website (<https://astrodeep.eu>).

## 2. Dataset

In this Section we summarize the properties of the dataset we used to obtain the set of photometric catalogs.

For all the fields but ABELL2744, we collected the NIRCам 30mas mosaics created by the teams of each program. In most cases, ancillary *HST* images were also made available; when

**Table 1:** Details of the pipeline versions and calibration files used for each dataset.

Dataset	DR	CRDS_VER	CRDS_CTX	CAL_VER
ABELL2744*	2.0	11.17.2	1183	1.11.3
CEERS DR0.5**	0.5	11.16.14	0989	1.7.2
CEERS DR0.6**	0.6	11.16.16	1023	1.8.5
JADES-GN	1.0	11.17.6	1130	1.11.4
JADES-GS	2.0	11.17.6	1132	1.11.4
NGDEEP SW	0.2b	11.16.15	1045	1.9.2
NGDEEP LW	0.3	11.17.0	1084	1.10.2
PRIMER- COSMOS	0.8	11.17.0	1123	1.10.2
PRIMER-UDS	0.6	11.17.0	1118***	1.10.2

\*GLASS-JWST, UNCOVER, DDT2756 and GO3390

\*\*CEERS full field mosaics are constructed from two separate public data releases: DR0.5 for NIRCам pointings 1,2,3,6 and DR0.6 for NIRCам pointings 4,5,7,8,9,10 (DOI 10.17909/z7p0-8481)

\*\*\*pmap 1117 for F356W, F410M, F444W

needed, we re-projected them on the same grid of the NIRCам mosaics, and checked for astrometric consistency (see Sect. B.1). All of the images were also scaled to  $\mu$ Jy units, so that AB magnitudes can be obtained from the flux measurements applying a constant zero-point (ZP) of 23.9. In the following we detail the process case by case; because of the composite nature of the dataset, which comprises images reduced by different teams at different times, the specific parameters of the reduction processes were unavoidably non-uniform. The different calibration files and pipeline versions that have been used are summarized in Table 1.

In order to create a formally homogeneous set of catalogs, we selected a fixed set of pass-band filters, thus also facilitating the photo- $z$  estimates for which tailored libraries of models are required. The chosen bands are: *HST* ACS F435W, F606W, F775W and F814W; *HST* WFC3 F105W, F125W, F140W and F160W; and NIRCам F090W, F115W, F150W, F200W, F277W, F356W, F410M and F444W. The main features of these pass-bands are summarized in Table 2. Note that not all of the bands are available in all fields; we provide the relevant details in the following subsections. The areas given for each field are indicative, as many pass-bands have different sky coverage; the values refer to the F444W band area.

### 2.1. ABELL2744

Imaging data from four programs have been combined in a single set of mosaics: GLASS-JWST (ERS 1324, P.I. Treu; no F410M, Treu et al. 2022), UNCOVER (GO 2561, P.I. Labbé; no F090W, Bezanson et al. 2022), DDT 2756 (P.I. Chen; no F090W and F410M), and GO 3990 (P.I. Morishita; no F410M). The resulting combined field of view (FoV) is centered on the galaxy cluster, and covers an area of  $\approx 45.7$  sq. arcmin. With respect to P23, new data have been received and added: the GO 3990 images in the UNCOVER region, and a new set of observations of the GLASS-JWST region acquired in July 2023 to correct the original 2022 images which were affected by a wing-tilt event in the short-wavelength bands (SW hereafter, i.e. F090W, F115W, F150W and F200W; the redder bands are denoted long-wavelength, LW hereafter). The reduction has been

**Table 2:** Main features of the pass-band filters included in the catalogs.  $fr$  is the fraction of the flux within a circular aperture of diameter  $0.2''$ . Wavelengths are given in nanometers; FWHMs are given in arcseconds.

Filter	$\lambda_{\text{ref}}$	$\lambda_{\text{mean}}$	$\lambda_{\text{eff}}$	FWHM	$fr_{0.2}$
HST ACS					
F435W	432.9	436.0	434.2	0.112	0.657
F606W	592.2	603.6	580.9	0.122	0.629
F775W	769.3	773.1	765.2	0.111	0.638
F814W	804.6	812.9	797.3	0.100	0.541
HST WFC3					
F105W	1055.0	1065.1	1043.1	0.162	0.371
F125W	1248.6	1257.6	1236.4	0.181	0.359
F140W	1392.3	1406.2	1373.5	0.178	0.320
F160W	1537.0	1543.6	1527.8	0.182	0.310
JWST NIRCам					
F090W	902.2	908.3	898.5	0.056	0.701
F115W	1154.3	1162.4	1143.4	0.059	0.716
F150W	1659.2	1786.6	1479.4	0.059	0.714
F200W	1988.6	2002.8	1968.0	0.073	0.686
F277W	2761.7	2784.5	2727.9	0.124	0.602
F356W	3568.4	3593.4	3528.7	0.146	0.553
F410M	4082.2	4088.7	4072.3	0.155	0.516
F444W	4404.3	4439.4	4350.4	0.166	0.496

re-done from scratch with new calibration files, following the procedure described in P23. The raw uncal images have been retrieved from the MAST archive<sup>1</sup>, and combined to cal images by applying the first two stages of the official *JWST* calibration pipeline (`calwebb_detector1` and `calwebb_image2`) with the latest calibration and reference files available to date, see Tab. 1. We then applied our modified version of the official pipeline using a number of custom procedures developed by our team to correct for defects – *snowballs*, non-linear pixels,  $1/f$ -noise, *wisps* and *claws* – and finally combined the calibrated images into mosaics and ancillary weight and error (root mean square, RMS) maps (see P23 Sect. 2.2.1 for details). We then complemented the NIRCам dataset with archival *HST* mosaics, reduced and publicly released by G. Brammer<sup>2</sup>.

We point out that this field is different from all the others, in that it is centered on a galaxy cluster. Working on this same region for the Frontier Fields campaign, Merlin et al. (2016b) developed a sophisticated technique to accurately subtract bright foreground galaxies and intra-cluster light from all the analysed bands. However, such a technique is complex and time-consuming, so we postpone its application to future work. As mentioned in P23, the global background and  $1/f$ -noise subtraction techniques effectively removes most of the intra-cluster light from the images. Furthermore, we provide photometric estimates including local background subtraction (see Sect. 3.4), which effectively removes residual intra-cluster light while also mitigating spurious effects created by the global processing. Nevertheless, we warn the users that the sources close to the center of the cluster should be treated with caution (see also Sect. 5); also, potential very high redshift objects magnified by (but close to) the cluster center are currently impossible to detect.

## 2.2. CEERS

Data from the CEERS program (ERS 1345, P.I. Finkelstein; no F090W, Finkelstein et al. 2022) cover an area of  $\approx 94.6$  sq. arcmin. Images have been reduced by M. Bagley combining two epochs of observations (see Bagley et al. 2023). The individual pointings are available from CEERS public releases 0.5 and 0.6<sup>3</sup>, and at MAST as High Level Science Products via DOI 10.17909/z7p0-8481. We have drizzled all ten individual pointings from these two releases into single mosaics for this paper. For *HST* we used the EGS dataset from CANDELS (Stefanon et al. 2017, no F435W and F775W data), with the addition of the F105W band from the CEERS HDR1 reduction<sup>4</sup>. A new catalog on a more recent, improved reduction of the NIRCам data, and obtained applying slightly different techniques, is going to be published soon by the CEERS team (Cox et al., in preparation).

## 2.3. JADES and NGDEEP

Data from the JADES program (GTO 1180, P.I. Eisenstein, and GTO 1210, P.I. Luetzgendorf, Eisenstein et al. 2023) cover an area of  $\approx 83.0$  sq. arcmin in the GOODS-North region (JADES-GN hereafter), and of  $\approx 84.5$  sq. arcmin in the GOODS-South region (JADES-GS hereafter). The images are available to the public and we used the v2.0 version for JADES-GS and the v1.0 version for JADES-GN. We complemented the NIRCам data using the Hubble Legacy Fields images (Illingworth et al. 2016).

The NGDEEP program (P.I. Finkelstein; no F090W and F410M, Bagley et al. 2024) adds an area of  $\approx 9.5$  sq. arcmin from the outer ECDFS area (with a marginal overlap with the GOODS-South field). Since the observed FoV does not overlap with JADES-GS, we kept the two fields separated, creating two catalogs and analysing them individually. We used the same imaging data of Leung et al. (2023), which only includes the first epoch of observation. This first epoch suffered from a lack in depth due to the DEEP8 readout pattern with a small number of groups. An updated catalog based on both significant improvements on the first epoch and including the second epoch will be published soon (Leung et al., in preparation).

## 2.4. PRIMER-COSMOS and PRIMER-UDS

Data is from the PRIMER program (GO 1837, P.I. Dunlop; no F775W for PRIMER-COSMOS and no F775W and F105W for PRIMER-UDS). The COSMOS FoV has an area of  $\approx 141.8$  sq. arcmin, and the UDS FoV has an area of  $\approx 251.2$  sq. arcmin. The images have been reduced by D. Magee, with *HST* data re-reduced from the CANDELS imaging.

## 3. Methods

In this Section we summarize the techniques and algorithms we used to prepare the images and extract the photometric information.

### 3.1. Alignment and astrometry

We assessed the quality of the astrometric registration by cross-matching the source coordinates ALPHAWIN\_J2000 and

<sup>1</sup> <https://mast.stsci.edu/>

<sup>2</sup> <https://s3.amazonaws.com/grizli-v2/JwstMosaics/v4/index.html>

<sup>3</sup> <https://ceers.github.io/dr05.html>,

<https://ceers.github.io/dr06.html>

<sup>4</sup> <https://ceers.github.io/releases#hdr1>

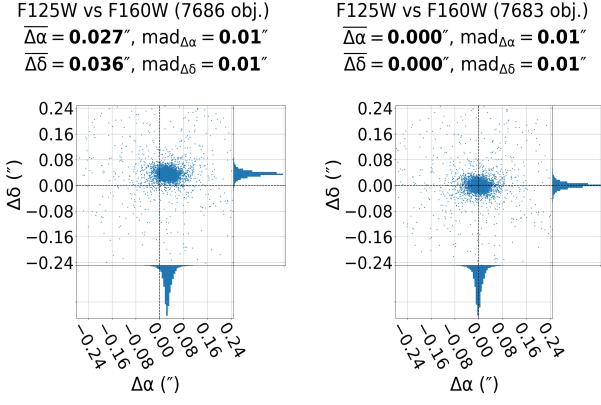


**Fig. 1:** Example of the validation tests made to fix the astrometric registration of the *HST* bands. Shown is the displacement  $\Delta\alpha$  and  $\Delta\delta$  between the sources detected in the CEERS F125W image and those detected in the CANDELS EGS F160W image, re-aligned to the reference frame of the CEERS F150W image, before (left panel) and after (right panel) applying the correction described in Section 3.1.

DELTAWIN\_J2000 obtained running SEXTRACTOR (Bertin & Arnouts 1996) on all the bands in each field before re-projecting the images to the same common grid. In most cases we found small  $\Delta\alpha$  and  $\Delta\delta$  offsets (of the order of a few mas) between the native astrometry of the *JWST* and the *HST* bands. However, since in some cases the offsets were larger and not negligible, we applied a custom algorithm to correct all of them. First, we computed the offset between the *HST* WFC3 F160W band and the *JWST* NIRC2 F150W band, and re-aligned the F160W image. Then we corrected the offsets of the other *HST* bands by cross-matching the coordinates of the sources with those extracted from the re-aligned F160W band (see Figure 1 and Tab. B.1 in Appendix). Finally, we re-projected all the images on the same NIRC2 pixel grid.

### 3.2. RMS scaling

Because the photometric errors are computed by means of the RMS maps (see Sect. 3.4), we checked that the latter were indeed representative of the true uncertainties of the measurement, using an improved version of the technique described in M22. In short, the RMS image of each band was subdivided into 2 to 4 complementary sub-regions of comparable exposure time, by means of an automatic algorithm applied to the weight maps. Then, in each of these sub-region 300 artificial point sources (WebbPSF simulated point spread functions) were injected at random positions, excluding areas assigned to real sources by means of SEXTRACTOR segmentation maps, and the dispersion of their fluxes (measured within an aperture of  $0.1''$  using the software A-phot, Merlin et al. 2019) was compared to their nominal errors to obtain a re-scaling factor for that region of the RMS map. Finally, the original map – which includes Poissonian photon noise – was then re-scaled by the median value of such factors. The typical values for SW bands are below  $\sim 1.5$ , while they can get as high as  $\sim 2.0$  for some LW bands and fields.

The histograms in Fig. D.1 show the distribution of the limiting magnitudes (total at  $5\sigma$  in apertures of  $0.2''$ ) for all the NIRC2 bands, as obtained from the re-scaled RMS map pixel values by means of the formula

$$\text{depth}_{5\sigma,i} = -2.5 \times \log(5 \times \sqrt{A} \times \text{RMS}_i / f_{r0.2}) + \text{ZP}, \quad (1)$$

**Table 3:** SEXTRACTOR parameters used for the detection.

Parameter	Value
DETECT_MINAREA	5
DETECT_THRESH	0.65/0.55/0.85*
ANALYSIS_THRESH	0.65/0.55/0.85*
DEBLEND_THRESH	32
DEBLEND_MINCONT	0.0003
MEMORY_OBJSTACK	50,000
MEMORY_PIXSTACK	10,000,000
MEMORY_BUFSIZE	4096

\*ABELL2744: 0.55; PRIMER-COSMOS: 0.85; other fields: 0.65

**Table 4:** Number of detections in the six fields.

Field	Detections
ABELL2744	42,491
CEERS	82,547
JADES-GN	58,385
JADES-GS	73,638
NGDEEP	14,752
PRIMER-COSMOS	123,094
PRIMER-UDS	136,266
Total	531,173

where  $i$  is a pixel index, ZP is the zero-point of the image (23.9 in our case),  $A = \pi(0.5 \times 0.2/\text{ps})^2$  is the area of the circular aperture of  $0.2''$  diameter (ps is the pixel scale), and  $f_{r0.2}$  is the fraction of the flux of a point source enclosed in the aperture (see Table 2).

### 3.3. Detection

Because the catalogs are mainly designed for the study of the high redshift universe, major effort was put in optimizing the measurements of faint extended objects, rather than those of bright local galaxies or stars. The strategy is similar to that adopted in M22 and P23: we chose to detect in the infrared, smoothing the scientific image with a Gaussian convolution filter with FWHM =  $0.14''$  (close to the F356W and F444W FWHMs, see below), and applying a detection threshold corresponding to  $\text{SNR} \sim 2$ , to pick up as many faint high redshift sources as possible. However, there is a substantial difference with respect to previous work: rather than just using F444W as detection band, we create a weighted stack of F356W and F444W, allowing to single out sources that peak at  $3.5$  to  $4 \mu\text{m}$ , and exploiting the F356W mosaics which are often as deep as, or deeper than, the F444W ones (see Appendix D). The resulting depths of the detection stacks are shown in Fig. 2.

We then run SEXTRACTOR v2.8.6, in the customised version used for the CANDELS campaign. Most of the parameters were left to the default values, with the exception of those given in Table 3. We tried to use the same values for all fields, but we found that DETECT\_THRESH and ANALYSIS\_THRESH needed adjustment in some cases, to ensure optimal results. In particular, we set them to 0.85 for PRIMER-COSMOS, and to 0.55 for ABELL2744; these values yielded the best trade-off between purity and completeness, allowing for the detection of faint sources while avoiding too many spurious objects to be included in the list.



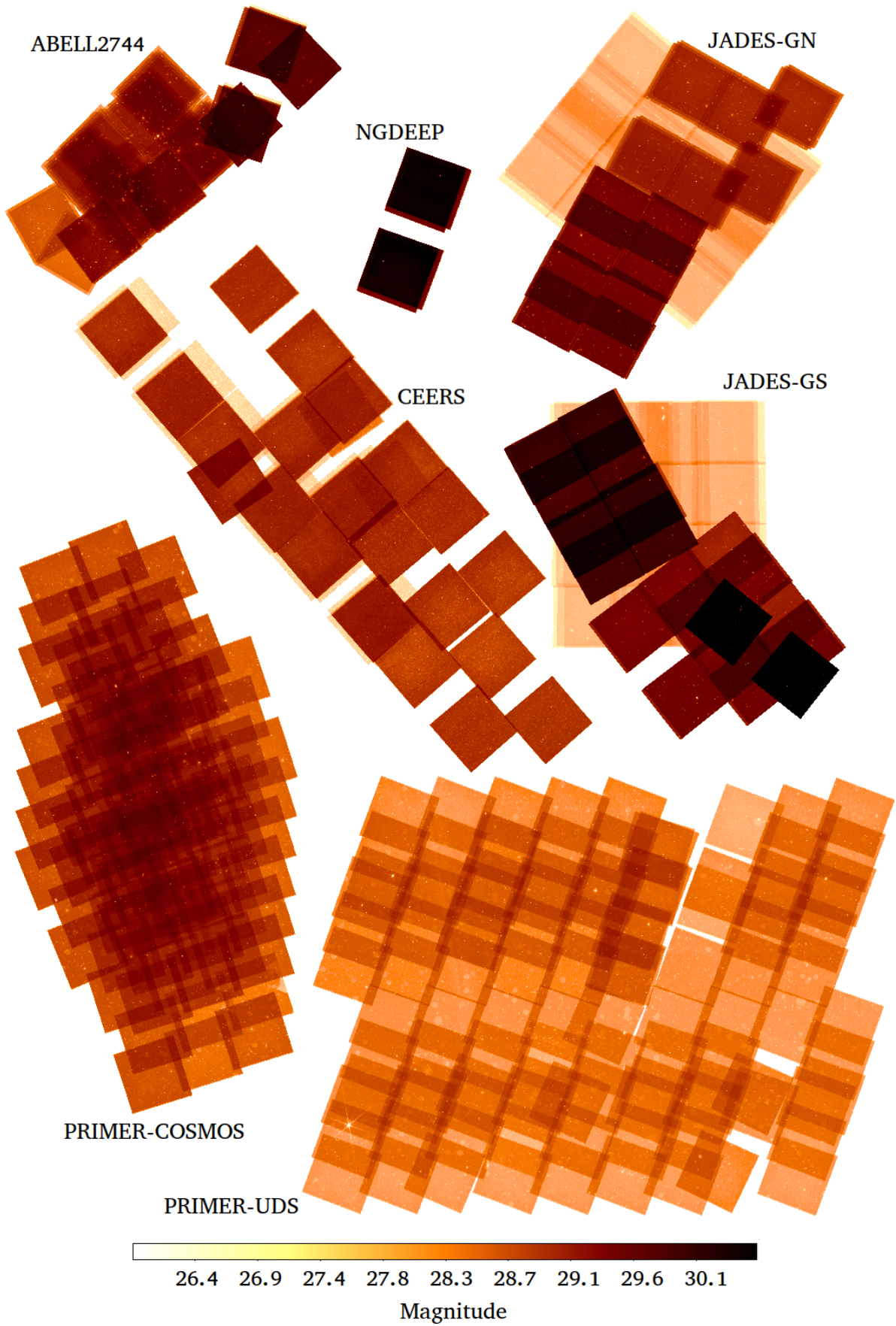


**Fig. 2:** Limiting magnitudes (total at  $5\sigma$  in  $0.2''$  diameter apertures) of the detection F356W+F444W stack mosaics.

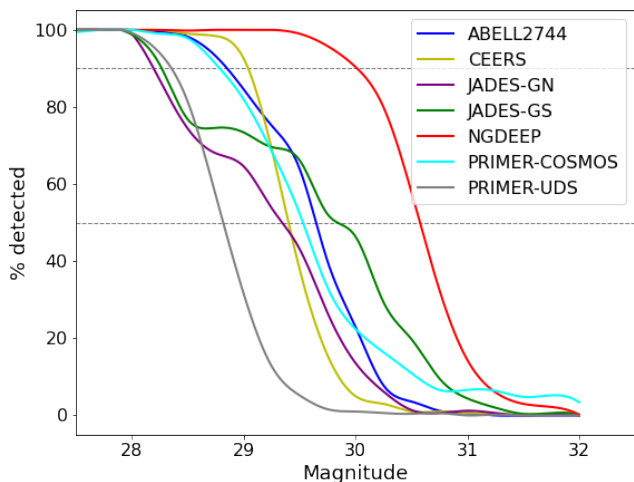


**Fig. 3:** Detection completeness. Shown is the fraction of fake point sources of given magnitude injected in the detection F356W+F444W stacks, and detected with SExtractor runs performed with the parameters used in real runs.

The final detection catalogs contain a grand total of 531,173 sources, as reported in Table 4. In the catalogs we include a unique object identifier number, the equatorial position (Right Ascension and declination, in degrees), and basic morphological information such as the area of the segmented cluster of pixels and the half light radius from SExtractor, and the semimajor axis, ellipticity and position angle of the elliptical isophote obtained by means of A-PHOT; see Appendix A for more details.

Fig. 3 shows the point-source detection completeness for the six fields, determined by injecting fake PSF-shaped objects in empty regions of the F356W+F444W stack (using the detection segmentation map as a mask), running SExtractor with the same parameters used in the actual detection process, and checking the fraction of them being actually detected. The different depths of the detection images is evident, NGDEEP being the deepest with 90% at  $AB \approx 30$  and 50% at  $AB \approx 30.5$ , and PRIMER-UDS the shallowest with 90% at  $AB \approx 28.5$  and 50% at  $AB \approx 29$ ; noticeable is the complicated pattern of the JADES-GS field, which comprises deep and shallow regions (90% completeness at  $AB \approx 28.5$  but 50% at  $AB \approx 30$ ).

### 3.4. Photometry

As in our previous efforts, in our public catalogs we provide total fluxes. The main methods used for this work are the same ones adopted in M22 and P23. In short, we compute colors from fixed circular apertures on PSF-matched images, and assuming no color gradients outside them we then re-scale to total fluxes multiplying them by the flux within Kron (1980) elliptical apertures in the F356W+F444W stack, as measured by the software A-PHOT (Merlin et al. 2019). So, the total flux in each band is given by the formula  $f_{tot,band} = c_{ap,det} \times f_{ap,band}$ , where  $c_{ap,det} = f_{tot,det}/f_{ap,det}$ . As pointed out in M22, our A-PHOT Kron-like aperture on average tends to gather more light than the standard SExtractor MAG\_AUTO (see Fig. 4 in M22), so we don't apply any further aperture correction to the total fluxes. Errors are estimated summing in quadrature the relevant pixels from the RMS maps and applying the same formula,  $e_{tot,band} = c_{ap,det} \times e_{ap,band}$ ; this choice is motivated by the fact that most scientific applications (e.g. SED-fitting or color-selections) are essentially based on colors, so the propagation of the total flux error would overes-

timate the relevant uncertainty. We compute fluxes within nine apertures (with diameters 0.2", 0.28", 0.33", 0.50", 0.66", 0.70", 1.32", 2.65" and 5.30"), and build just as many catalogs of total fluxes. The values of the apertures correspond to integer multiples of the F444W FWHM 0.165", except for the two smallest ones (a fixed 0.1" radius aperture and the value corresponding to the WebbPSF<sup>5</sup> F444W FWHM, 0.14") and the sixth one (corresponding to the larger aperture in the UNCOVER catalog by Weaver et al. 2024). We point out that we did not correct the fluxes for the cluster magnification effect in the ABELL2744 field.

For each field, we provide an “optimal” catalog, in which the total flux of each source is obtained from the colors computed in a preferred aperture chosen on the basis of the object segmentation area. We used SExtractor ISOAREA\_IMAGE as a proxy for it, and selected as the preferred aperture the one immediately larger than the value  $\sqrt{ISOAREA\_IMAGE/\pi}$  (this implies that the diameter of the optimal aperture is close to the radius of the circularized detected area). The value of this preferred aperture is also reported in the catalog.

#### 3.4.1. PSF models

A major difference with respect to our previous efforts is the usage of empirical PSFs rather than models simulated using the WebbPSF application. For each band, we created empirical models stacking isolated, high SNR stars, singled out visually after an automatic pre-selection performed using catalogs created with ad-hoc SExtractor runs on each band. After trying various options, among which using stars from each field to create the PSFs for that field only, we found that the best results in terms of growth curves and photometric vs. spectroscopic redshifts comparison (see Section 5) was to create an “über”-model for each band, stacking all the available good stars from all fields after rotating each one by the average position angle (PA) of the observation, and finally rotating back the obtained model to the PA of the considered field (we used the Python module `numpy.rotate` for this task). In the cases in which the observations are stacks of different epochs, we created models using the stars with the most common orientation in our selection (also considering those consisting of two superposed PSFs with different orientations), which typically sample the largest area in the field. Fig. 5 show the final PSF “über”-models before the final rotation for being used in the different fields.

#### 3.4.2. Background subtraction

A-PHOT can perform “on-the-fly” local background subtraction while measuring fluxes. Including this feature is not necessarily the best choice in all cases, as it may yield sub-optimal estimates close to bright sources or in densely populated regions; however, it is typically reasonable to apply it. Therefore, we release both sets of catalogs with the local background subtraction option switched on and off, but we suggest to use the background-subtracted catalogs as best choice. We checked that the difference is not dramatic for the vast majority of the sources, but it has an impact in some cases. Fig. 6 shows the difference in measured fluxes in six bands with and without A-PHOT background subtraction, in all fields: major differences can be seen around the bright galaxies in the ABELL2744 cluster (notice how the A-PHOT background subtraction makes the objects

<sup>5</sup> <https://www.stsci.edu/jwst/science-planning/proposal-planning-toolbox/psf-simulation-tool>

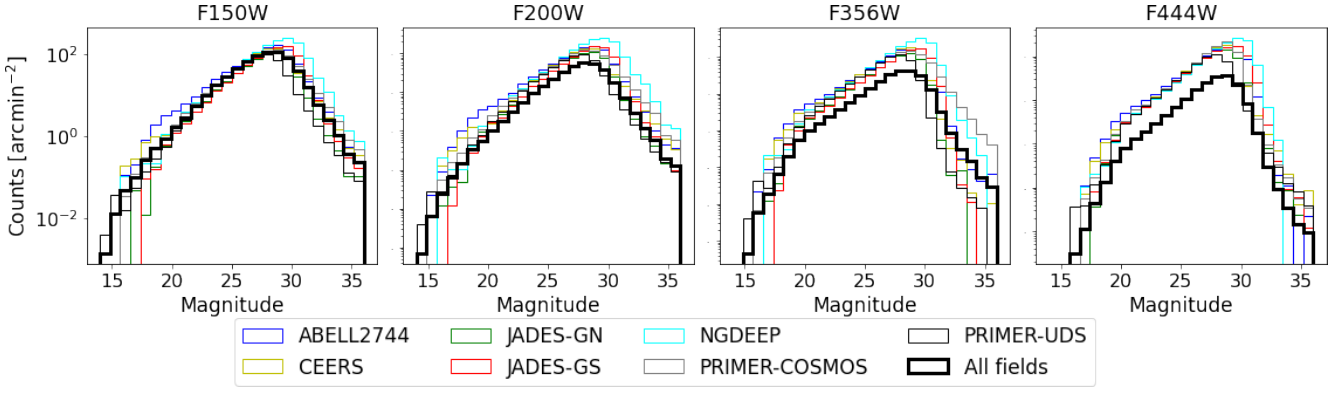


**Fig. 4:** Number counts in four NIRCcam bands (total magnitudes from the optimal catalogs, normalized to field area); black thick line is the total of all fields.

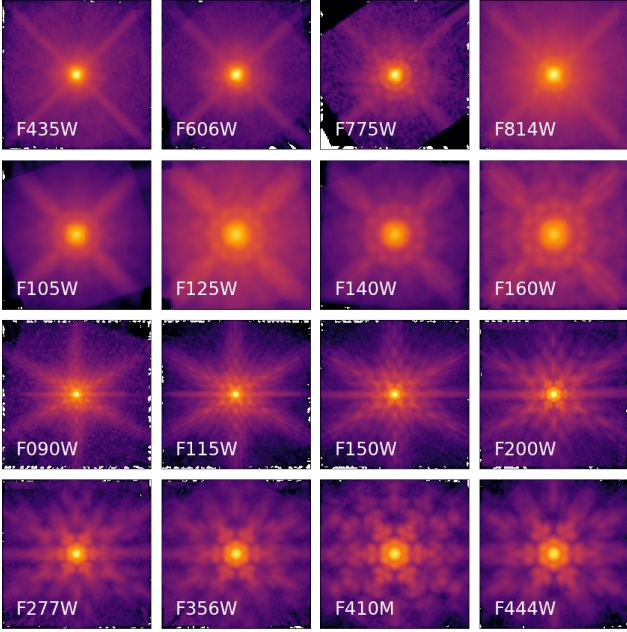


**Fig. 5:** PSF “über”-models for all the bands in the catalogs. See text for details.

closest to the cluster members fainter, but those slightly farther away brighter, compensating for over-subtraction in the image processing phase) and in an extended area of the PRIMER-UDS field.

### 3.4.3. Galactic extinction

We finally corrected all the total fluxes for the effects of galactic extinction, taking advantage of the calculator provided by the NASA/IPAC Extragalactic Database (NED)<sup>6</sup>, which gives the average dimming in each band at any given equatorial coordinates (we provide those corresponding to the center of the FoVs of the fields). We use such values to compute the extinction-corrected fluxes, and use the latter for the final catalogs.

Fig. 4 shows the number counts of all fields in four bands using the magnitudes obtained using the total fluxes in the “optimal” catalog and after the correction for galactic extinction. Comparing it with Fig. 3, it can be seen that the counts in the F444W and F356W bands typically peak close to the 50% com-

<sup>6</sup> [https://ned.ipac.caltech.edu/extinction\\_calculator](https://ned.ipac.caltech.edu/extinction_calculator)

**Table 5:** Flags assigned in the catalogs. The final flag is the sum of the individual flagging values.

Flag	Description
+1-8	Source is missing <i>HST</i> bands
+10-80	Source is missing <i>JWST</i> bands
+100	Source is contaminated by close neighbors, or has bad pixels in detection
+200	Source is blended with another in detection
+400	Source is saturated in detection
+800	Source is close to a border
+10,000	Point-like
+20,000	All <i>HST</i> fluxes are negative
+40,000	Bad measurements in both F356W and F444W
+100,000	Spurious detection

pleteness detection magnitude, which is consistent with previous studies (see e.g. Guo et al. 2013, their Fig. 4).

### 3.5. Star/galaxy separation, spurious detections, and flagging

To identify and flag point-like sources and potentially spurious detections (PLS and PSD, respectively) we adopted a Principal Component Analysis (PCA) technique, described in details in Appendix C. In short, taking advantage of the quantities  $MU\_MAX$ ,  $MAG\_AUTO$ ,  $MAGERR\_AUTO$  and  $FLUX\_RADIUS$  estimated with SExtractor on the F356W+F444W detection stack, we obtained a 2-dimensional projection space in which PLS occupy an extremely well-defined and tight locus, and PSD gather in a relatively confined region. The first column of Fig. C.1 shows the resulting diagram for all the fields, with the inner subplot magnifying the region where spurious and regular sources overlap; the exact formulae used to isolate PLS and PSD in the diagram are given in Sect. C. The second and third columns show the position of the sources in two complementary diagnostic planes, i.e. the  $MU\_MAX - MAG\_AUTO$  plane and the  $FLUX\_RADIUS$  vs SNR plane, where PLS and PSD also occupy well-defined regions; the usage of the PCA approach allows for a more general identification, combining the two in a fluid way.

We then assigned a further flag to each source, based on the detection and photometric measurements. Table 5 describes the used values, the final flag being the sum of all the individual addenda. Power-of-two values multiplied by 100 are assigned on the basis of the detection measurements, as output by the A-



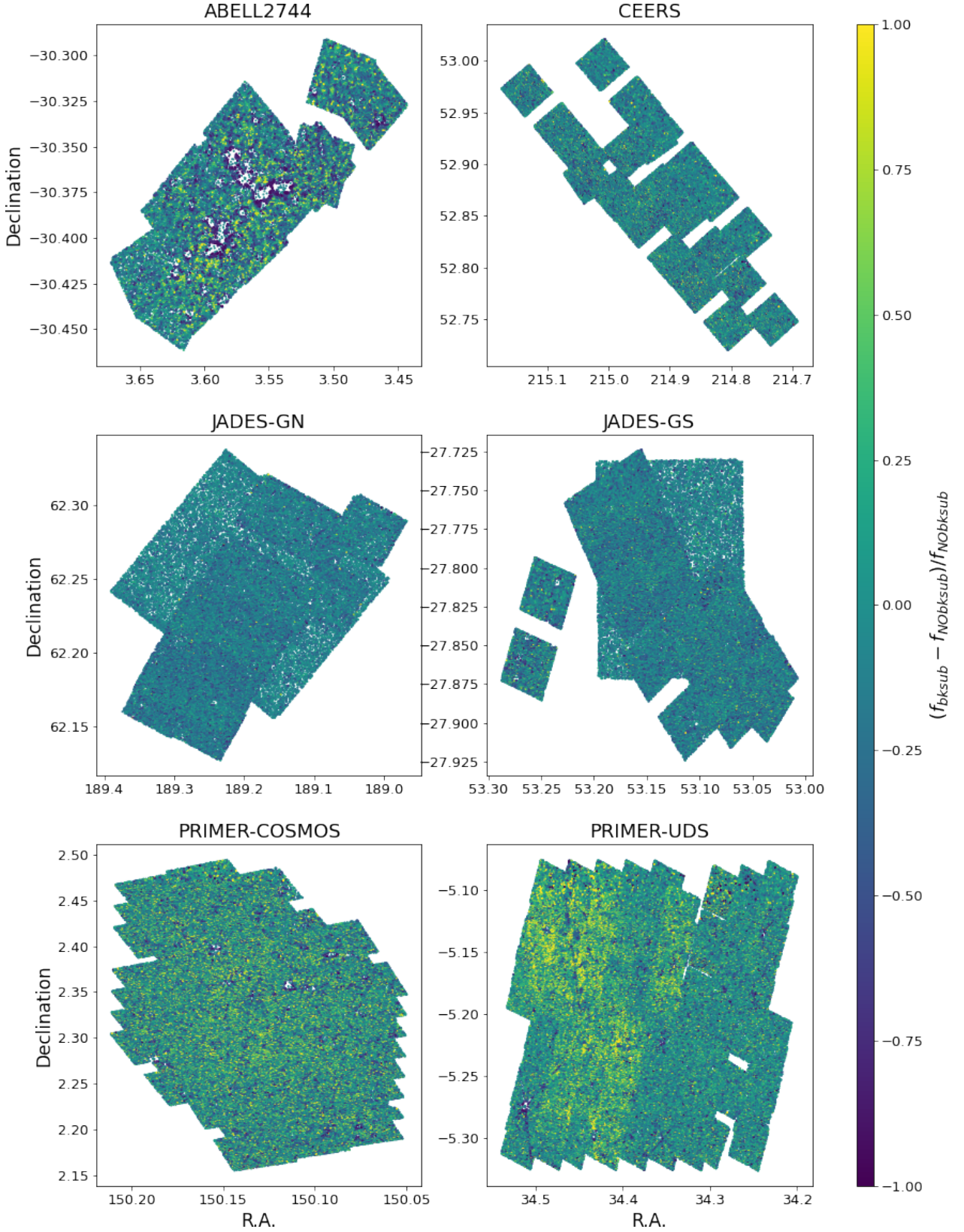


**Fig. 6:** Relative difference of measured fluxes in F444W with the  $\alpha$ -PHOT background subtraction switched on and off.

PHOT code, the maximum value being 1500; while addenda below 100 indicate the number of *HST* and/or *JWST* bands missing because of the different observational coverage of the areas. We also included a special flag for the sources with all *HST* measurement having negative values (a few sources in a limited region of

the ABELL2744 field, because of problematic background subtraction in the cluster core area). To give an example, a source flagged with the value 11016 identifies a point-like object, which is blended and saturated in the detection band, and has one *JWST* and six *HST* bands missing. Thus, a flag lower than 199 typically



indicates a “regular” galaxy-like source which might have missing bands and/or be contaminated in its detection total flux, but it is not blended in detection, not saturated, not close to the borders of the image, and not identified as a star or a spurious detection. Clearly, these flags are a useful diagnostic tool, but we suggest to use them with caution, as they are the result of many automatic processes that cannot be 100% accurate.

A certain number of spurious detections is unavoidably destined to remain in the catalogs. To further improve the purity, we visually checked all sources with photometric redshift estimate above 10 (see Sect. 5), to exclude at least the most obvious errors in this important sub-space of the catalogs. Doing so, we found that most remaining cases were defects in the detection stack, either caused by missing coverage in the F356W or F444W images, and/or by obvious reduction errors or noise features that were not singled out in the diagnostic planes. The most affected fields were ABELL2744, CEERS and PRIMER-UDS.

It is reasonable to assume that similar spurious detections could exist at photo- $z < 10$ , although detecting in the reddest bands favours high photometric redshift estimates for these kind of fake sources. However, since it would be impossible to go through all of the catalogs to find them, we invite the users to carefully inspect any objects selected for scientific purposes.

#### 4. Validation of photometry

To validate the accuracy of our catalogs, we compared our “optimal” catalogs (see Sect. 3.4) to other available ones, either published or obtained via private communication with the proprietary teams. We considered both archival catalogs based on *HST* observations (CANDELS and ASTRODEEP releases), and recent *JWST* catalogs from various research groups: P23 and Weaver et al. (2024) for ABELL2744, Finkelstein et al. (2023a) for CEERS, S. Finkelstein’s priv. comm. catalog for NGDEEP, and the JADES public catalogs for the two JADES fields, v2.0 for GOODS-South and v1.0 for GOODS-North (see Rieke et al. 2023)<sup>7</sup>.

We cross-matched the catalogs using the equatorial coordinates of the detected sources with a searching radius of 0.35". For the comparisons we only considered sources that have SNR > 5 in both catalogs, and flag < 200 in this work (i.e., well-behaved galaxies, non-blended in the detection stack; see Sect. 3.5).

Since many details about the detection procedure vary significantly because of the different techniques adopted in the various works, we choose to focus on colors rather than on total fluxes, as they convey a more robust diagnostic on the accuracy of the estimated SED of the galaxies. The results are shown in Figs. E.1 to E.6 (the last panel for each field shows the relative difference in the total flux in F444W for *JWST* catalogs and in F160W for *HST* catalogs, for the sake of completeness).

The agreement is generally good, in particular with *JWST* catalogs and especially in the NIRCам bands. The larger differences are found with respect to the P23 catalog for ABELL2744 in the *HST* bluer bands, most likely because of the different PSF models and the local background subtraction introduced in this work. We also notice a systematic trend with respect to the JADES catalogs in the *HST* bands, with our colors typically becoming larger towards the faint end of the distribution; given the good agreement of the F444W flux band estimates, this must be due to our fluxes being fainter in the *HST* bands. Concerning the

comparisons with the archival *HST* catalogs, we notice an evident declining trend at the faint end of most plots, which must be due to the deeper sensitivity of the *JWST* data. Faint objects are now measured with more accuracy, whereas in the old catalog they often happened to have spurious positive fluxes (higher than their nominal errors, thus not being classified as upper limits) as a result of local noise fluctuations, especially in the less resolved redder bands (*Ks* and IRAC), resulting in larger colors with respect to those measured in the high quality NIRCам images.

Furthermore, in the cases of ABELL2744 vs. the ASTRODEEP catalog by Merlin et al. (2016a) and NGDEEP vs. the CANDELS by Guo et al. (2013), the matched sources are very few, so the comparison is less significant.

We feel confident that most of the discrepancies can be explained considering the differences in the adopted processing techniques, in particular concerning the apertures used to measure the fluxes, the PSF models, the background subtraction algorithms, the correction for galactic extinction. Similar discrepancies have been found among multi-wavelength catalogs in past efforts (see e.g. Stefanon et al. 2017); a more detailed analysis is beyond the scope of the present work.

#### 5. Photometric redshifts

We estimated photometric redshifts on our “optimal” catalogs using the software packages ZPHOT (Fontana et al. 2000) and EAzy (Brammer et al. 2008).

For ZPHOT we adopted Bruzual & Charlot (2003) templates, assumed exponentially declining Star Formation Histories (SFH) with timescale  $\tau$  ranging from 0.1 to 15 Gyr, and included nebular emission lines according to Castellano et al. (2014) and Schaerer & de Barros (2009); metallicity can assume values of 0.02, 0.2, 1 and 2.5 times Solar and the age is allowed to vary from 10 Myr to the age of the Universe at a given redshift; finally, we adopted a Calzetti et al. (2000) extinction law with E(B-V) in the range 0–1.1.

For EAzy we made three runs, one with the pre-defined set of templates eazy\_v1.3 and the other two with the ones presented by Larson et al. (2023b) (we used the FSPS + Set 1 + Set 3 or “LyaReduced” and FSPS Set 1 + Set 4 or “Lya” combinations, as suggested by the authors; see <https://ceers.github.io/LarsonSEDTemplates>). So we end up with four redshift estimates, which we list in our final catalogs.

As a final test on our photometry, we checked the accuracy of the photometric redshifts estimates by considering the subsample of sources having spectroscopic information from the literature. We matched these spectroscopic targets with our catalogs adopting a conservative searching radius of 0.3". We considered the following spectroscopic samples: (i) NIRSpc: for ABELL2744, data from the programs GLASS-JWST-ERS-1324 (Treu et al. 2022), UNCOVER-GO-2561 (Bezanson et al. 2022) and GO-3073 (Castellano et al. 2024), using the Mascia et al. (2024) and Price et al. (2024, UNCOVER DR4) data releases, plus additional ones from our own on-going data analysis (Napolitano et al., in preparation); for CEERS, data from the program CEERS-ERS-1345 (Finkelstein et al. 2023a), retrieving them from the public DAWN JWST Archive<sup>8</sup> (see details in Heintz et al. 2024); for the JADES fields, data from the program JADES-GTO-1180 (Eisenstein et al. 2023), using the DR3 spectroscopic catalogs (D’Eugenio et al. 2024) released by the

<sup>7</sup> <https://archive.stsci.edu/hlsp/jades>

<sup>8</sup> <https://dawn-cph.github.io/dja>

team<sup>9</sup>. Additionally, we also included the collection of spectra from various programs analysed and listed in Roberts-Borsani et al. (2024), and more data from the DAWN JWST Archive as available at the moment of writing this paper (July 2024); (ii) CANDELSz7 (Pentericci et al. 2018b) data, for JADES-GS, NGDEEP, and PRIMER; (iii) VANDELS DR4 (Pentericci et al. 2018a; McLure et al. 2018; Garilli et al. 2021) data, for PRIMER-UDS, JADES-GS and NGDEEP; (iv) the collection of ground based spectroscopy obtained with different instruments by different projects (VIMOS, Braglia et al. 2009, and MUSE, Mahler et al. 2018; Richard et al. 2021; Bergamini et al. 2023a,b) at the VLT, AAOmega on the Anglo-Australian Telescope, Owers et al. 2011, and of the HST WFC3/IR grism through the HST GO program GLASS (Treu et al. 2015; Schmidt et al. 2014) for the ABELL27444 field; (v) the collection compiled by the CANDELS collaboration and described in Kodra et al. (2023) for CEERS, JADES-GN PRIMER-UDS, PRIMER-COSMOS; (vi) the updated compilation of Merlin et al. (2021) for JADES-GS and NGDEEP; (vii) additional redshifts from Cowie et al. (2004); Reddy et al. (2006); Trump et al. (2009); van der Wel et al. (2016); Inami et al. (2017); Damjanov et al. (2018); Straatman et al. (2018); Scodreggio et al. (2018); Masters et al. (2019); Wisnioski et al. (2019); Urrutia et al. (2019); Ning et al. (2020); Jones et al. (2021); Pharo et al. (2022); Bacon et al. (2023) and the redshifts collected by Grazian et al. (2006); Wuyts et al. (2008); Xue et al. (2011); (viii) the MUSE (Schmidt et al. 2021; Rosani et al. 2020), zCOSMOS (Lilly et al. 2007), DEIMOS (Hasinger et al. 2018), VUDS (Tasca et al. 2017) catalogs for PRIMER-COSMOS. For our final comparisons we only included robust redshifts estimates on the basis of the various quality flags provided the authors, and took care to avoid repetitions. Whenever a spectroscopic target is listed in more than one survey and the inferred redshift estimates (flagged as robust) differ by more than  $0.05 \times (1 + z_{avg})$ , where  $z_{avg}$  is the average spectroscopic redshift, we removed the target from the sample; if the difference is lower than this value but larger than 0.1, we considered the redshift, but we conservatively removed it from the statistics adopted to evaluate the accuracy of our photometric redshifts (see below).

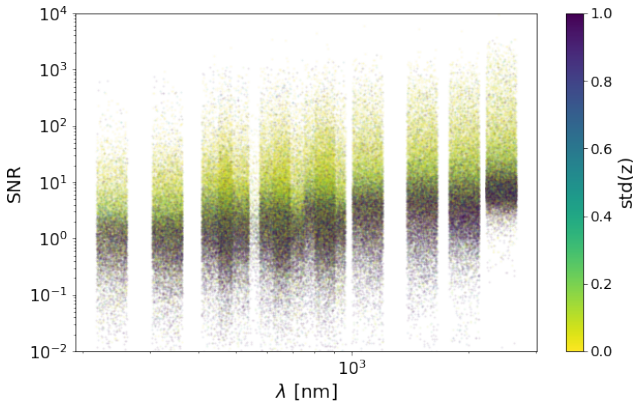


**Fig. 7:** Comparative accuracy of photometric redshift estimates as a function of the SNR of the sources. The plot shows, for a random sample of 10,000 sources from the PRIMER-COSMOS field, the SNR at the wavelengths corresponding to the photometric bands included in the catalog, color-coding each point with the standard deviation of three photo- $z$  estimates. Objects with  $SNR < 10$  in the red bands (and/or  $SNR < 1$  in the blue bands) tend to have discordant photo- $z$  estimates. See text for more details)

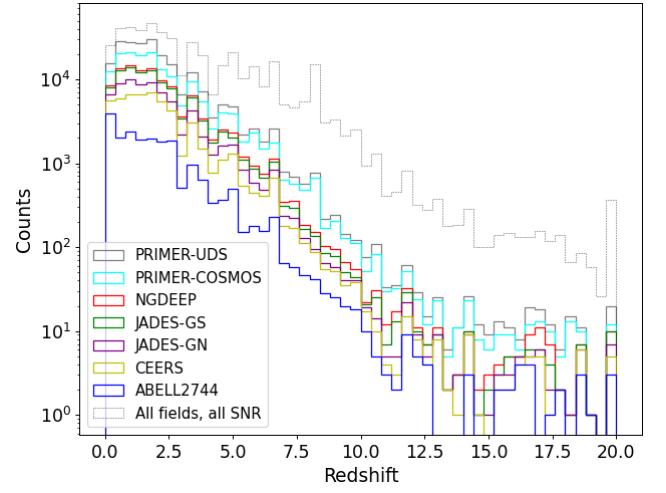


**Fig. 8:** Distribution of the median photometric redshifts obtained with the runs described in Sect. 5. Stacked coloured histograms refer to individual fields, showing only sources with  $SNR_{F356W+F444W} > 10$  and flag  $< 400$ ; the dotted black lines shows the cumulative distribution for all fields, including all SNRs. The inner panel magnifies the distribution at  $z > 10$ .

Since the templates do not include an AGN component, to correctly evaluate the accuracy of the inferred photometric redshifts we removed known AGNs from the catalogues, regardless of their nuclear contribution to the galaxy SED. To this aim, we took advantage of the samples presented by Harikane et al. (2023), Goulding et al. (2023), Maiolino et al. (2023), Kocevski et al. (2023), Larson et al. (2023a), Roberts-Borsani et al. (2024), Greene et al. (2024), Barro et al. (2024), based on JWST data, of X-ray catalogs (Nandra et al. 2015; Xue et al. 2016; Luo et al. 2017; Kocevski et al. 2018) by flagging as AGN all sources with 2-10 keV luminosity larger than  $10^{42}$  erg/s or identified as AGN by the authors, and we removed spectroscopic targets flagged as AGNs from the VANDELS, zCOSMOS, DEIMOS, VUDS and COSMOS2020 (Weaver et al. 2022) datasets.

Finally, we removed from the lists problematic sources using the flags described in Sect. 3.5. In particular, we excluded spurious detections, stars, sources that are saturated or at the boundary of the images - that is, we only kept sources with flag  $< 400$ ; in addition, we removed sources missing JWST photometry in more than three bands (i.e. having the tens figure in the flag larger than 3). With this criteria, we are left with a total sample of 16,263 spectra.

Fig. F.1 shows, for the total of the sources and for each field separately, the comparisons between the spectroscopic redshifts and the median values of the photo- $z$  estimates. The latter were computed excluding the EAZY “LyA” run (to avoid over-weighting the results from the runs using the templates by Larson, which are very similar in the two cases). Tab. F.1 reports the full statistics for the four runs made with zPHOT and EAZY. We define  $dz = |z_{phot} - z_{spec}| / (1 + z_{spec})$ , and  $f_{outliers}$  as the percentage of objects with  $dz < 0.15$ ; we then compute mean, median, standard deviation, and NMAD (defined as  $1.48 \times \text{median}(|dz|)$ ) of non-outliers. The four runs yield comparable statistics. The overall accuracy of the median estimates is good (NMAD 0.031, standard deviation 0.041 considering all fields together), and better than that from any individual zPHOT or EAZY run. There is a non-negligible fraction of outliers (6.3%) comparable to, albeit larger than, the one reached in recent efforts on multi-wavelength catalogs with a larger number of bands (and more sophisticated approaches, see e.g. Merlin et al. 2021). Looking at Fig. F.1

<sup>9</sup> <https://jades-survey.github.io/scientists/data.html>

we also note that the accuracy varies from field to field, with ABELL2744 and NGDEEP having the largest outlier fractions, most likely because of the effect of the cluster on photometric measurements for the former and of the low number of available spectroscopic redshifts for the latter.

We report that we also tested delayed exponentially declining SFHs with the *z*PHOT code, and verified that our choice of standard exponentially declining models performs better in terms of agreement with spectroscopic redshifts.

We point out that the photometric redshift estimates are prone to substantial uncertainties for the sources at low SNR. Fig. 7 exemplifies this by showing, for a random sub-sample of 10,000 sources in the PRIMER-COSMOS catalog, the value of the standard deviation of the photo-*z* estimates obtained with three runs<sup>10</sup>, as a function of the detection SNR in all bands: clearly, the discrepancy grows with decreasing SNR. Since we detected in the reddest bands, sources close to the detection limit in the F356W+F444W stack typically become even fainter in bluer images, thus making their characterization very hard, as different codes and/or templates prefer different solutions for poorly constrained photometry.

Then, as discussed in Sect. 3.5, taking the *z*PHOT runs as reference (given its overall slightly better performance) we also visually inspected all of the sources with estimated redshift above 10 (which were initially 7224). By doing so, not only did we exclude a further population of spurious detections, but we identified some systematic cases in which the redshift estimate was wrong due to unfortunate lack of relevant data: for example, in PRIMER-UDS some sources have been observed only with the LW NIRC*am* filters, and the missing information at wavelengths blue-ward of F277W caused a wrong identification of the Lyman break and therefore of the redshift. We marked these and similar cases with a negative sign before the flag value in the photometric redshifts catalogs. After these checks, we were left with 3101 objects with photo-*z* > 10. This number is certainly an over-estimation. Indeed, only 922 have standard deviation of the estimates of the three codes lower than 0.5, again highlighting the challenging task of robustly constraining the photometric redshift for such faint, distant sources. Furthermore, some red low redshift interlopers must be present (see Arrabal Haro et al. 2023b; Harikane et al. 2024), and we deliberately only removed clearly spurious detections, not the uncertain or suspect ones – so certainly there are still fake sources polluting the sample. Comparing e.g. with the estimated surface density of high-*z* objects by Finkelstein et al. (2023b, their Fig. 8), we would expect ~20 galaxies at *z* > 10 with F277W < 28.5 in CEERS; we find 65 in the *z*PHOT sample (a value close to the expected number after correcting for completeness), but just 14 considering a restricted sample of sources having the standard deviation of the estimates from the three codes lower than 0.5.

Having clarified this, Fig. 8 shows the final distributions of the estimated redshifts (median estimate). The colored stacked histograms refer to the individual fields and show the distribution of sources with detection SNR > 10 and not flagged as point-like, spurious, or with a bad redshift estimate because of lacking bands, as previously explained. The dotted thin black line shows the total distribution including all SNRs. The discussed issues lead to some evidently artificial features in the global photo-

*z* distribution, which largely disappear when considering only high SNR (e.g., SNR<sub>F444W</sub> > 10) sources. A thorough comparative analysis of the probability distribution functions (PDF) from the four runs would be needed to disentangle the degeneracy for the faint objects, but this goes beyond the scope of this work, so we restrict ourselves to releasing the output of the runs. For similar reasons we also postpone the release of the physical properties for the galaxies (see e.g. Markov et al. 2023).

## 6. Summary and conclusions

We presented and discussed a major release of photometric catalogs, collecting data from eight *JWST* observational programs on six deep extra-galactic fields. We release a new reduction of the Abell 2744 composite mosaics, gathering the GLASS-JWST, UNCOVER, DDT2756 and GO3990 programs, and use the reductions provided by the teams of the other programs. NIRC*am* data are complemented with archival *HST* images on which we perform new measurements.

The catalogs, mainly conceived for high redshift science, include a grand-total of 531,173 objects, of which 17,359 are tagged as spurious, and 2,268 more have bad photometric measurements (flag ≥ 400, see Section 3.5). Sources were detected with SExtractor on stacks of the F356W and F444W mosaics of each field. For all the detections we provide positions in equatorial and pixel coordinates, basic morphological parameters, total fluxes and corresponding uncertainties in 16 photometric bands computed by means of the software *λ*-PHOT, a diagnostic flag, and four photometric redshift estimates obtained with *z*PHOT and EA*z*Y.

We performed validation tests on the astrometry, the photometry and the photo-*z* accuracy, comparing our catalogs against other releases and finding a general good agreement.

The catalogs are available for download from the ASTRODEEP website, <https://astrodeep.eu>. Updates and/or additional releases will be documented on the website and uploaded to the same repository. We encourage the community to exploit these catalogs for any suitable scientific purpose.

**Acknowledgements.** This work is based in part on observations made with the NASA/ESA/CSA James Webb Space Telescope. The data were obtained from the Mikulski Archive for Space Telescopes at the Space Telescope Science Institute, which is operated by the Association of Universities for Research in Astronomy, Inc., under NASA contract NAS 5-03127 for *JWST*. These observations are associated with program *JWST*-ERS-1342.

This research is also based in part on observations made with the NASA/ESA Hubble Space Telescope obtained from the Space Telescope Science Institute, which is operated by the Association of Universities for Research in Astronomy, Inc., under NASA contract NAS 5-26555. These observations are associated with program *HST*-GO-17321.

This research is also supported in part by the Australian Research Council Centre of Excellence for All Sky Astrophysics in 3 Dimensions (ASTRO 3D), through project number CE170100013.

We also acknowledge support from the INAF Large Grant 2022 “Extragalactic Surveys with *JWST*” (PI Pentericci).

B.V. is supported by the European Union – NextGenerationEU RFF M4C2 1.1 PRIN 2022 project 2022ZSL4BL INSIGHT.

## References

- Adamo, A., Atek, H., Bagley, M. B., et al. 2024, arXiv e-prints, arXiv:2405.21054
- Arrabal Haro, P., Dickinson, M., Finkelstein, S. L., et al. 2023a, *ApJ*, 951, L22
- Arrabal Haro, P., Dickinson, M., Finkelstein, S. L., et al. 2023b, *Nature*, 622, 707
- Bacon, R., Brinchmann, J., Conseil, S., et al. 2023, *A&A*, 670, A4
- Bagley, M. B., Finkelstein, S. L., Koekemoer, A. M., et al. 2023, *ApJ*, 946, L12
- Bagley, M. B., Pirzkal, N., Finkelstein, S. L., et al. 2024, *ApJ*, 965, L6

<sup>10</sup> We computed the median and standard deviation of the estimates using the runs made with *z*PHOT, EA*z*Y with *eazy\_v1.3* templates, and EA*z*Y with Larson FSPS + Set 1 + Set 4 templates; we did not include the run with Larson FSPS + Set 1 + Set 3 templates since it yielded very similar results to the other one.

- Barro, G., Pérez-González, P. G., Kocevski, D. D., et al. 2024, *ApJ*, 963, 128
- Bergamini, P., Acebron, A., Grillo, C., et al. 2023a, *A&A*, 670, A60
- Bergamini, P., Acebron, A., Grillo, C., et al. 2023b, *ApJ*, 952, 84
- Bertin, E. & Arnouts, S. 1996, *A&AS*, 117, 393
- Bezanson, R., Labbe, I., Whitaker, K. E., et al. 2022, *arXiv e-prints*, arXiv:2212.04026
- Braglia, F. G., Pierini, D., Biviano, A., & Böhringer, H. 2009, *A&A*, 500, 947
- Brammer, G. B., van Dokkum, P. G., & Coppi, P. 2008, *ApJ*, 686, 1503
- Bruzual, G. & Charlot, S. 2003, *MNRAS*, 344, 1000
- Calzetti, D., Armus, L., Bohlin, R. C., et al. 2000, *ApJ*, 533, 682
- Carnall, A. C., McLeod, D. J., McLure, R. J., et al. 2023, *MNRAS*, 520, 3974
- Carniani, S., Hainline, K., D'Eugenio, F., et al. 2024, *arXiv e-prints*, arXiv:2405.18485
- Castellano, M., Fontana, A., Treu, T., et al. 2023, *ApJ*, 948, L14
- Castellano, M., Fontana, A., Treu, T., et al. 2022, *arXiv e-prints*, arXiv:2207.09436
- Castellano, M., Napolitano, L., Fontana, A., et al. 2024, *arXiv e-prints*, arXiv:2403.10238
- Castellano, M., Sommariva, V., Fontana, A., et al. 2014, *A&A*, 566, A19
- Ciesla, L., Elbaz, D., Ilbert, O., et al. 2023, *arXiv e-prints*, arXiv:2309.15720
- Cowie, L. L., Barger, A. J., Hu, E. M., Capak, P., & Songaila, A. 2004, *AJ*, 127, 3137
- Damjanov, I., Zahid, H. J., Geller, M. J., Fabricant, D. G., & Hwang, H. S. 2018, *ApJS*, 234, 21
- Davis, K., Trump, J. R., Simons, R. C., et al. 2023, *arXiv e-prints*, arXiv:2312.07799
- Davis, M., Guhathakurta, P., Konidaris, N. P., et al. 2007, *ApJ*, 660, L1
- Dekel, A., Sarkar, K. C., Birnboim, Y., Mandelker, N., & Li, Z. 2023, *MNRAS*, 523, 3201
- D'Eugenio, F., Cameron, A. J., Scholtz, J., et al. 2024, *arXiv e-prints*, arXiv:2404.06531
- Dressler, A., Vulcani, B., Treu, T., et al. 2023, *ApJ*, 947, L27
- Eisenstein, D. J., Willott, C., Alberts, S., et al. 2023, *arXiv e-prints*, arXiv:2306.02465
- Ferrara, A., Pallottini, A., & Dayal, P. 2023, *MNRAS*, 522, 3986
- Finkelstein, S. L., Bagley, M. B., Arrabal Haro, P., et al. 2022, *ApJ*, 940, L55
- Finkelstein, S. L., Bagley, M. B., Ferguson, H. C., et al. 2023a, *ApJ*, 946, L13
- Finkelstein, S. L., Leung, G. C. K., Bagley, M. B., et al. 2023b, *arXiv e-prints*, arXiv:2311.04279
- Fontana, A., D'Odorico, S., Poli, F., et al. 2000, *AJ*, 120, 2206
- Galametz, A., Grazian, A., Fontana, A., et al. 2013, *ApJS*, 206, 10
- Gardner, J. P., Mather, J. C., Abbott, R., et al. 2023, *PASP*, 135, 068001
- Gardner, J. P., Mather, J. C., Clampin, M., et al. 2006, *Space Sci. Rev.*, 123, 485
- Garilli, B., McLure, R., Pentericci, L., et al. 2021, *A&A*, 647, A150
- Giacconi, R., Zirm, A., Wang, J., et al. 2002, *ApJS*, 139, 369
- Giavalisco, M., Ferguson, H. C., Koekemoer, A. M., et al. 2004, *ApJ*, 600, L93
- Glazebrook, K., Nanayakkara, T., Jacobs, C., et al. 2023, *ApJ*, 947, L25
- Goulding, A. D., Greene, J. E., Setton, D. J., et al. 2023, *ApJ*, 955, L24
- Grazian, A., Fontana, A., de Santis, C., et al. 2006, *A&A*, 449, 951
- Greene, J. E., Labbe, I., Goulding, A. D., et al. 2024, *ApJ*, 964, 39
- Grogin, N. A., Kocevski, D. D., Faber, S. M., et al. 2011, 197, 35
- Guo, Y., Ferguson, H. C., Giavalisco, M., et al. 2013, 207, 24
- Harikane, Y., Nakajima, K., Ouchi, M., et al. 2024, *ApJ*, 960, 56
- Harikane, Y., Zhang, Y., Nakajima, K., et al. 2023, *ApJ*, 959, 39
- Hasinger, G., Capak, P., Salvato, M., et al. 2018, *ApJ*, 858, 77
- Heintz, K. E., Brammer, G. B., Watson, D., et al. 2024, *arXiv e-prints*, arXiv:2404.02211
- Illingworth, G., Magee, D., Bouwens, R., et al. 2016, *arXiv e-prints*, arXiv:1606.00841
- Inami, H., Bacon, R., Brinchmann, J., et al. 2017, *A&A*, 608, A2
- Jacobs, C., Glazebrook, K., Calabrò, A., et al. 2023, *ApJ*, 948, L13
- Jones, L. H., Rosenthal, M. J., Barger, A. J., & Cowie, L. L. 2021, *ApJ*, 916, 46
- Kartaltepe, J. S., Rose, C., Vanderhoof, B. N., et al. 2023, *ApJ*, 946, L15
- Kirkpatrick, A., Yang, G., Le Bail, A., et al. 2023, *ApJ*, 959, L7
- Kocevski, D. D., Hasinger, G., Brightman, M., et al. 2018, *ApJS*, 236, 48
- Kocevski, D. D., Onoue, M., Inayoshi, K., et al. 2023, *ApJ*, 954, L4
- Kodra, D., Andrews, B. H., Newman, J. A., et al. 2023, *ApJ*, 942, 36
- Koekemoer, A. M., Faber, S. M., Ferguson, H. C., et al. 2011, *ApJS*, 197, 36
- Kokorev, V., Caputi, K. I., Greene, J. E., et al. 2024, *ApJ*, 968, 38
- Kron, R. G. 1980, *ApJS*, 43, 305
- Larson, R. L., Finkelstein, S. L., Kocevski, D. D., et al. 2023a, *ApJ*, 953, L29
- Larson, R. L., Hutchison, T. A., Bagley, M., et al. 2023b, *ApJ*, 958, 141
- Lawrence, A., Warren, S. J., Almaini, O., et al. 2007, *MNRAS*, 379, 1599
- Leung, G. C. K., Bagley, M. B., Finkelstein, S. L., et al. 2023, *ApJ*, 954, L46
- Lilly, S. J., Le Fèvre, O., Renzini, A., et al. 2007, *ApJS*, 172, 70
- Looser, T. J., D'Eugenio, F., Maiolino, R., et al. 2023, *arXiv e-prints*, arXiv:2306.02470
- Lotz, J., Mountain, M., Grogin, N. A., et al. 2014, in *American Astronomical Society Meeting Abstracts*, Vol. 223, American Astronomical Society Meeting Abstracts #223, 254.01
- Luo, B., Brandt, W. N., Xue, Y. Q., et al. 2017, *ApJS*, 228, 2
- Mahler, G., Richard, J., Clément, B., et al. 2018, *MNRAS*, 473, 663
- Maiolino, R., Scholtz, J., Curtis-Lake, E., et al. 2023, *arXiv e-prints*, arXiv:2308.01230
- Markov, V., Gallerani, S., Pallottini, A., et al. 2023, *A&A*, 679, A12
- Mascia, S., Pentericci, L., Calabrò, A., et al. 2024, *A&A*, 685, A3
- Mason, C. A., Trenti, M., & Treu, T. 2023, *MNRAS*, 521, 497
- Masters, D. C., Stern, D. K., Cohen, J. G., et al. 2019, *ApJ*, 877, 81
- McLeod, D. J., Donnan, C. T., McLure, R. J., et al. 2024, *MNRAS*, 527, 5004
- McLure, R. J., Pentericci, L., Cimatti, A., et al. 2018, *MNRAS*, 479, 25
- Merlin, E., Amorín, R., Castellano, M., et al. 2016a, *A&A*, 590, A30
- Merlin, E., Bonchi, A., Paris, D., et al. 2022, *ApJ*, 938, L14
- Merlin, E., Bourne, N., Castellano, M., et al. 2016b, *A&A*, 595, A97
- Merlin, E., Castellano, M., Santini, P., et al. 2021, *A&A*, 649, A22
- Merlin, E., Fortuni, F., Torelli, M., et al. 2019, *MNRAS*, 490, 3309
- Naidu, R. P., Oesch, P. A., van Dokkum, P., et al. 2022, *ApJ*, 940, L14
- Nanayakkara, T., Glazebrook, K., Jacobs, C., et al. 2024, *Scientific Reports*, 14, 3724
- Nandra, K., Laird, E. S., Aird, J. A., et al. 2015, *ApJS*, 220, 10
- Nayyeri, H., Hemmati, S., Mobasher, B., et al. 2017, *ApJS*, 228, 7
- Ning, Y., Jiang, L., Zheng, Z.-Y., et al. 2020, *ApJ*, 903, 4
- Oke, J. B. & Gunn, J. E. 1983, *ApJ*, 266, 713
- Owers, M. S., Randall, S. W., Nulsen, P. E. J., et al. 2011, *ApJ*, 728, 27
- Padmanabhan, H. & Loeb, A. 2023, *ApJ*, 953, L4
- Paris, D., Merlin, E., Fontana, A., et al. 2023, *ApJ*, 952, 20
- Pentericci, L., McLure, R. J., Garilli, B., et al. 2018a, *A&A*, 616, A174
- Pentericci, L., Vanzella, E., Castellano, M., et al. 2018b, *A&A*, 619, A147
- Pérez-González, P. G., Barro, G., Annunziatella, M., et al. 2023a, *ApJ*, 946, L16
- Pérez-González, P. G., Barro, G., Rieke, G. H., et al. 2024, *ApJ*, 968, 4
- Pérez-González, P. G., Costantin, L., Langeroodi, D., et al. 2023b, *ApJ*, 951, L1
- Pharo, J., Guo, Y., Calvo, G. B., et al. 2022, *ApJS*, 261, 12
- Price, S. H., Bezanson, R., Labbe, I., et al. 2024, *arXiv e-prints*, arXiv:2408.03920
- Reddy, N. A., Steidel, C. C., Erb, D. K., Shapley, A. E., & Pettini, M. 2006, *ApJ*, 653, 1004
- Richard, J., Claeysens, A., Lagattuta, D., et al. 2021, *A&A*, 646, A83
- Rieke, M. J., Robertson, B., Tacchella, S., et al. 2023, *ApJS*, 269, 16
- Roberts-Borsani, G., Treu, T., Shapley, A., et al. 2024, *arXiv e-prints*, arXiv:2403.07103
- Rodighiero, G., Enia, A., Bisigello, L., et al. 2024, *arXiv e-prints*, arXiv:2405.04572
- Rosani, G., Caminha, G. B., Caputi, K. I., & Deshmukh, S. 2020, *A&A*, 633, A159
- Santini, P., Fontana, A., Castellano, M., et al. 2023, *ApJ*, 942, L27
- Schaerer, D. & de Barros, S. 2009, *A&A*, 502, 423
- Schmidt, K. B., Kerutt, J., Wisotzki, L., et al. 2021, *A&A*, 654, A80
- Schmidt, K. B., Treu, T., Brammer, G. B., et al. 2014, *ApJ*, 782, L36
- Scodreggio, M., Guzzo, L., Garilli, B., et al. 2018, *A&A*, 609, A84
- Stefanon, M., Yan, H., Mobasher, B., et al. 2017, *ApJS*, 229, 32
- Straatman, C. M. S., van der Wel, A., Bezanson, R., et al. 2018, *ApJS*, 239, 27
- Tasca, L. A. M., Le Fèvre, O., Ribeiro, B., et al. 2017, *A&A*, 600, A110
- Treu, T., Calabrò, A., Castellano, M., et al. 2023, *ApJ*, 942, L28
- Treu, T., Roberts-Borsani, G., Bradac, M., et al. 2022, *ApJ*, 935, 110
- Treu, T., Schmidt, K. B., Brammer, G. B., et al. 2015, *ApJ*, 812, 114
- Trinca, A., Schneider, R., Valiante, R., et al. 2024, *MNRAS*, 529, 3563
- Trump, J. R., Impey, C. D., Elvis, M., et al. 2009, *ApJ*, 696, 1195
- Urrutia, T., Wisotzki, L., Kerutt, J., et al. 2019, *A&A*, 624, A141
- van der Wel, A., Noeske, K., Bezanson, R., et al. 2016, *ApJS*, 223, 29
- Wang, B., Leja, J., de Graaff, A., et al. 2024, *arXiv e-prints*, arXiv:2405.01473
- Ward, E., de la Vega, A., Mobasher, B., et al. 2024, *ApJ*, 962, 176
- Weaver, J. R., Cutler, S. E., Pan, R., et al. 2024, *ApJS*, 270, 7
- Weaver, J. R., Kauffmann, O. B., Ilbert, O., et al. 2022, *ApJS*, 258, 11
- Weibel, A., Oesch, P. A., Barrufet, L., et al. 2024, *arXiv e-prints*, arXiv:2403.08872
- Williams, C. C., Alberts, S., Ji, Z., et al. 2024, *ApJ*, 968, 34
- Wisnioski, E., Förster Schreiber, N. M., Fossati, M., et al. 2019, *ApJ*, 886, 124
- Wright, L., Whitaker, K. E., Weaver, J. R., et al. 2024, *ApJ*, 964, L10
- Wuyts, S., Labbé, I., Förster Schreiber, N. M., et al. 2008, *ApJ*, 682, 985
- Xue, Y. Q., Luo, B., Brandt, W. N., et al. 2016, *ApJS*, 224, 15
- Xue, Y. Q., Luo, B., Brandt, W. N., et al. 2011, *ApJS*, 195, 10
- Yung, L. Y. A., Somerville, R. S., Finkelstein, S. L., Wilkins, S. M., & Gardner, J. P. 2024, *MNRAS*, 527, 5929



- <sup>1</sup> INAF – Osservatorio Astronomico di Roma, Via Frascati 33, 00078 Monteporzio Catone, Rome, Italy  
e-mail: emiliano.merlin@inaf.it
- <sup>2</sup> Department of Physics and Astronomy, University of California, Los Angeles, 430 Portola Plaza, Los Angeles, CA 90095, USA
- <sup>3</sup> Department of Astronomy, The University of Texas at Austin, Austin, TX, USA
- <sup>4</sup> SUPA<sup>11</sup>, Institute for Astronomy, University of Edinburgh, Royal Observatory, Edinburgh EH9 3HJ, UK
- <sup>5</sup> NSF’s National Optical-Infrared Astronomy Research Laboratory, 950 N. Cherry Ave., Tucson, AZ 85719, USA
- <sup>6</sup> School of Physics, University of Melbourne, Parkville 3010, VIC, Australia
- <sup>7</sup> ARC Centre of Excellence for All Sky Astrophysics in 3 Dimensions (ASTRO 3D), Australia
- <sup>8</sup> Space Science Data Center, Italian Space Agency, via del Politecnico, 00133, Roma, Italy
- <sup>9</sup> Department of Physics, 196A Auditorium Road, Unit 3046, University of Connecticut, Storrs, CT 06269, USA<sup>12</sup>
- <sup>10</sup> Space Telescope Science Institute, Baltimore, MD, USA
- <sup>11</sup> University of Massachusetts, 710 N. Pleasant St, LGRB-520, Amherst, MA 01003, USA
- <sup>12</sup> Centre for Astrophysics and Supercomputing, Swinburne University of Technology, PO Box 218, Hawthorn, VIC 3122, Australia
- <sup>13</sup> INAF – Osservatorio Astronomico di Padova, Vicolo Osservatorio 5, 35122 Padova, Italy
- <sup>14</sup> Institute of Physics, Lab for Galaxy Evolution, EPFL, Observatoire de Sauverny, Chemin Pegasi 51, 1290 Versoix, Switzerland
- <sup>15</sup> Laboratory for Multiwavelength Astrophysics, School of Physics and Astronomy, Rochester Institute of Technology, 84 Lomb Memorial Drive, Rochester, NY 14623, USA
- <sup>16</sup> Center for Astrophysics | Harvard & Smithsonian, 60 Garden Street, Cambridge, MA 02138, USA
- <sup>17</sup> Department of Physics and Astronomy, University of Kansas, Lawrence, KS 66045, USA
- <sup>18</sup> Department of Physics and Astronomy, Colby College, Waterville, ME 04901, USA
- <sup>19</sup> Department of Astronomy and Astrophysics, UCO/Lick Observatory, University of California, Santa Cruz CA 95064, USA
- <sup>20</sup> Department of Physics & Astronomy, Tufts University, MA 02155, USA
- <sup>21</sup> Dipartimento di Fisica, Università di Roma Sapienza, Città Universitaria di Roma - Sapienza, Piazzale Aldo Moro, 2, 00185, Roma, Italy
- <sup>22</sup> INAF – Osservatorio Astronomico di Trieste, Via Tiepolo 11, I-34131 Trieste, Italy
- <sup>23</sup> Department of Physics and Astronomy, Texas A&M University, College Station, TX, 77843-4242 USA
- <sup>24</sup> George P. and Cynthia Woods Mitchell Institute for Fundamental Physics and Astronomy, Texas A&M University, College Station, TX, 77843-4242 USA
- <sup>25</sup> Centro de Astrobiología (CAB), CSIC-INTA, Ctra. de Ajalvir km 4, Torrejón de Ardoz, E-28850, Madrid, Spain
- <sup>26</sup> ESA/AURA Space Telescope Science Institute
- <sup>27</sup> Astrophysics Science Division, NASA Goddard Space Flight Center, 8800 Greenbelt Road, Greenbelt, MD 20771, USA
- <sup>28</sup> Center for Research and Exploration in Space Science and Technology II, Department of Physics, Catholic University of America, 620 Michigan Ave N.E., Washington DC 20064, USA
- <sup>29</sup> Department of Astronomy, University of Geneva, Chemin Pegasi 51, 1290 Versoix, Switzerland
- <sup>30</sup> Center for Computational Astrophysics, Flatiron Institute, 162 5th Avenue, New York, NY 10010, USA
- <sup>31</sup> School of Astronomy and Space Science, University of Chinese Academy of Sciences (UCAS), Beijing 100049, China
- <sup>32</sup> National Astronomical Observatories, Chinese Academy of Sciences, Beijing 100101, China
- <sup>33</sup> Institute for Frontiers in Astronomy and Astrophysics, Beijing Normal University, Beijing 102206, China
- <sup>34</sup> Astronomy Centre, University of Sussex, Falmer, Brighton BN1 9QH, UK
- <sup>35</sup> Institute of Space Sciences and Astronomy, University of Malta, Msida MSD 2080, Malta
- <sup>36</sup> Kapteyn Astronomical Institute, University of Groningen, P.O. Box 800, 9700 AV Groningen, The Netherlands
- <sup>37</sup> SRON Netherlands Institute for Space Research, Postbus 800, 9700 AV Groningen, The Netherlands

## Appendix A: Catalog format

We release several catalogs for each field, among which one (named “optap”-catalog) is obtained assigning to each source the colors computed in its “optimal” aperture (see Sect. 3.4). The catalogs are published in `fits` format, and come with a `README` file that explains the meaning and format of the columns. All catalogs first list a set of columns indicating the unique identifiers of the detected objects, their position in equatorial coordinates and in pixels, and some values from the `SExtractor` detection run on the F356W+F444W stack mosaics: `ISOAREA_IMAGE`, `CLASS_STAR`, `FLAGS`, `FLUX_RADIUS`, `FLUX_AUTO`, `FLUXERR_AUTO`. Then, some measures obtained with `A-phot` again on the detection stack: the major semi-axis of the elliptical isophote, the ellipticity and the position angle, and the Kron radius (in pixels). The total fluxes in the 16 photometric bands, computed as described in Sect. 3.4, are then given, followed by the corresponding 16 uncertainties (all in  $\mu\text{Jy}$  units). Finally, the last column lists the flags discussed in Sect. 3.5. In the “optap”-catalog the value of the “optimal” aperture is also given (in arcseconds).

We separately release a set of photometric redshifts catalogs estimated on the “optap”-catalog with local background subtraction. For each source they list the ID, RA and Dec, the spectroscopic redshift when available, the four estimates of the photometric redshift (see Sect. 5), and the flag assigned to the source as reported also in the “optap”-catalog, with the additional indication of a negative sign for the sources lacking information in the bands necessary to identify the Lyman break.

## Appendix B: Astrometry

As explained in Sect. 3.1, we re-aligned *HST* mosaics to NIR-Cam grid by means of an automatic procedure. Table B.1 lists the offsets in RA and Dec after the procedure, for all the bands and fields. We point out that the CANDELS EGS and CEERS HDR1 *HST* data are obtained from the same observations, but the latter has been re-aligned to Gaia-DR3; since we took care to correct all of the images for astrometric accuracy, the two datasets should be perfectly consistent.

**Table B.1:** The median and MAD of the astrometric offsets of the *HST* bands, computed cross-matching the sources and corrected before re-projecting the *HST* images to the JWST grid. For each field, the F160W values are the coordinate offsets between the original *HST* F160W and the NIRCам F150W band, while the others refer to the offsets between the given band and F160W band after it was re-aligned to the F150W.

Target	Band	$N_{obj}$	$\Delta RA$ (")	$\Delta DEC$ (")
ABELL2744	F435W	1307	$0.009 \pm 0.02$	$0.000 \pm 0.01$
	F606W	3309	$0.001 \pm 0.02$	$0.001 \pm 0.01$
	F814W	3188	$-0.001 \pm 0.02$	$-0.001 \pm 0.01$
	F105W	4595	$0.003 \pm 0.01$	$0.001 \pm 0.01$
	F125W	2170	$0.003 \pm 0.02$	$-0.001 \pm 0.01$
	F140W	849	$0.005 \pm 0.02$	$0.003 \pm 0.01$
	F160W	2054	$0.003 \pm 0.02$	$0.000 \pm 0.01$
CEERS	F606W	7063	$0.044 \pm 0.03$	$0.032 \pm 0.02$
	F814W	8615	$0.066 \pm 0.02$	$0.041 \pm 0.01$
	F105W	1437	$0.007 \pm 0.05$	$0.010 \pm 0.03$
	F125W	7686	$0.027 \pm 0.01$	$0.036 \pm 0.01$
	F160W	4355	$0.064 \pm 0.05$	$0.040 \pm 0.02$
JADES-GN	F435W	1144	$0.036 \pm 0.05$	$0.015 \pm 0.02$
	F606W	1822	$0.045 \pm 0.04$	$0.015 \pm 0.02$
	F814W	3228	$0.040 \pm 0.03$	$0.015 \pm 0.01$
	F105W	2800	$0.041 \pm 0.02$	$0.012 \pm 0.01$
	F125W	3430	$0.039 \pm 0.01$	$0.013 \pm 0.00$
	F140W	1532	$0.044 \pm 0.01$	$0.015 \pm 0.01$
	F160W	1436	$0.041 \pm 0.04$	$0.013 \pm 0.02$
JADES-GS	F435W	13997	$0.006 \pm 0.03$	$-0.015 \pm 0.03$
	F606W	21408	$0.004 \pm 0.02$	$-0.012 \pm 0.02$
	F814W	19677	$0.000 \pm 0.02$	$-0.010 \pm 0.01$
	F105W	12169	$0.005 \pm 0.01$	$-0.013 \pm 0.01$
	F125W	18764	$0.007 \pm 0.01$	$-0.013 \pm 0.01$
	F140W	8542	$0.008 \pm 0.01$	$-0.014 \pm 0.01$
	F160W	6235	$0.006 \pm 0.03$	$-0.013 \pm 0.02$
NGDEEP	F435W	758	$0.082 \pm 0.04$	$-0.058 \pm 0.03$
	F606W	1194	$0.077 \pm 0.03$	$-0.052 \pm 0.03$
	F775W	1121	$0.077 \pm 0.03$	$-0.052 \pm 0.03$
	F814W	1096	$0.079 \pm 0.03$	$-0.053 \pm 0.02$
	F105W	815	$0.091 \pm 0.01$	$-0.049 \pm 0.01$
	F125W	965	$0.091 \pm 0.01$	$-0.050 \pm 0.01$
	F160W	506	$0.089 \pm 0.02$	$-0.049 \pm 0.02$
PRIMER-COSMOS	F435W	733	$0.010 \pm 0.04$	$0.012 \pm 0.05$
	F606W	1279	$-0.011 \pm 0.03$	$-0.022 \pm 0.03$
	F814W	2925	$-0.004 \pm 0.01$	$-0.008 \pm 0.01$
	F125W	4704	$-0.004 \pm 0.01$	$-0.011 \pm 0.01$
	F140W	2797	$-0.006 \pm 0.01$	$-0.006 \pm 0.02$
	F160W	3709	$-0.005 \pm 0.02$	$-0.011 \pm 0.02$
PRIMER-UDS	F435W	1214	$0.008 \pm 0.04$	$0.000 \pm 0.04$
	F606W	3613	$-0.003 \pm 0.03$	$0.010 \pm 0.03$
	F814W	4779	$-0.003 \pm 0.03$	$0.009 \pm 0.03$
	F125W	3911	$0.010 \pm 0.01$	$-0.004 \pm 0.01$
	F140W	1653	$0.010 \pm 0.02$	$-0.004 \pm 0.02$
	F160W	4915	$0.010 \pm 0.03$	$-0.005 \pm 0.04$

### Appendix C: Selection of stars and potentially spurious sources

The PCA technique described in Sect. 3.5 works as follows. We fed the `scikit-learn` module `decomposition.PCA` with three parameters from the `SEXTRACTOR` detection catalog, i.e. the signal-to-noise ratio `SNR` obtained as the ratio between `FLUX_AUTO` and `FLUXERR_AUTO`, the peak surface brightness above background `MUMAX`, and the half light radius `FLUX_RADIUS`. We used a subsample of the `PRIMER-COSMOS` `SEXTRACTOR` detection catalog to determine the principal components matrix  $[[0.38283975 \ 0.65126842 \ 0.65519704],$

$[0.92363354 \ -0.28388812 \ -0.25750461]]$  (with explained variance ratio  $[0.65961785 \ 0.27738227]$ ), and then applied this matrix to the full catalogs of all fields. The loci of PLS and PSS are easily identified in the resulting principal components diagram, and after a rigid anti-clockwise rotation of  $66.5^\circ$  PSS can be singled out by a simple law,  $0.15 < \text{rPCA2} < 0$  &  $\text{rPCA2} < c_{st}$  (where  $\text{rPCA}i$  indicates the value of the rotated component). PSS can be identified as those in the uppermost region of the diagram, using the law  $\text{rPC2} > c_{sp1} \times \log_{10}(1 + \text{rPC1}) + c_{sp2}$  &  $\text{rPC1} > c_{sp3}$ . The exact definition of the locus of the two populations slightly varies from field to field, as shown by the values of the constants reported in Table C.1.

We point out that this approach joins two similar and complementary techniques using diagnostic diagrams to identify the loci occupied by point-like and spurious sources, i.e. the SNR vs radius plane and the  $\mu$ -mag vs mag plane. Fig. C.1 shows the PCA plane for all fields in the left column, and the two diagrams corresponding to the other techniques in the central and right columns.

**Table C.1:** Constants used to single out stars and potentially spurious objects in the rotated PCA plane.

Field	$c_{st}$	$c_{sp1}$	$c_{sp2}$	$c_{sp3}$
ABELL2744	0.5	0	1.75	-0.2
CEERS	0.5	3	2	-10
JADES-GN	0.8	3	2	-10
JADES-GS	0.5	5	2.5	-10
NGDEEP	0.8	3	2	-10
PRIMER-COSMOS	0.5	0	2.2	-0.2
PRIMER-UDS	0.5	0	2	-10



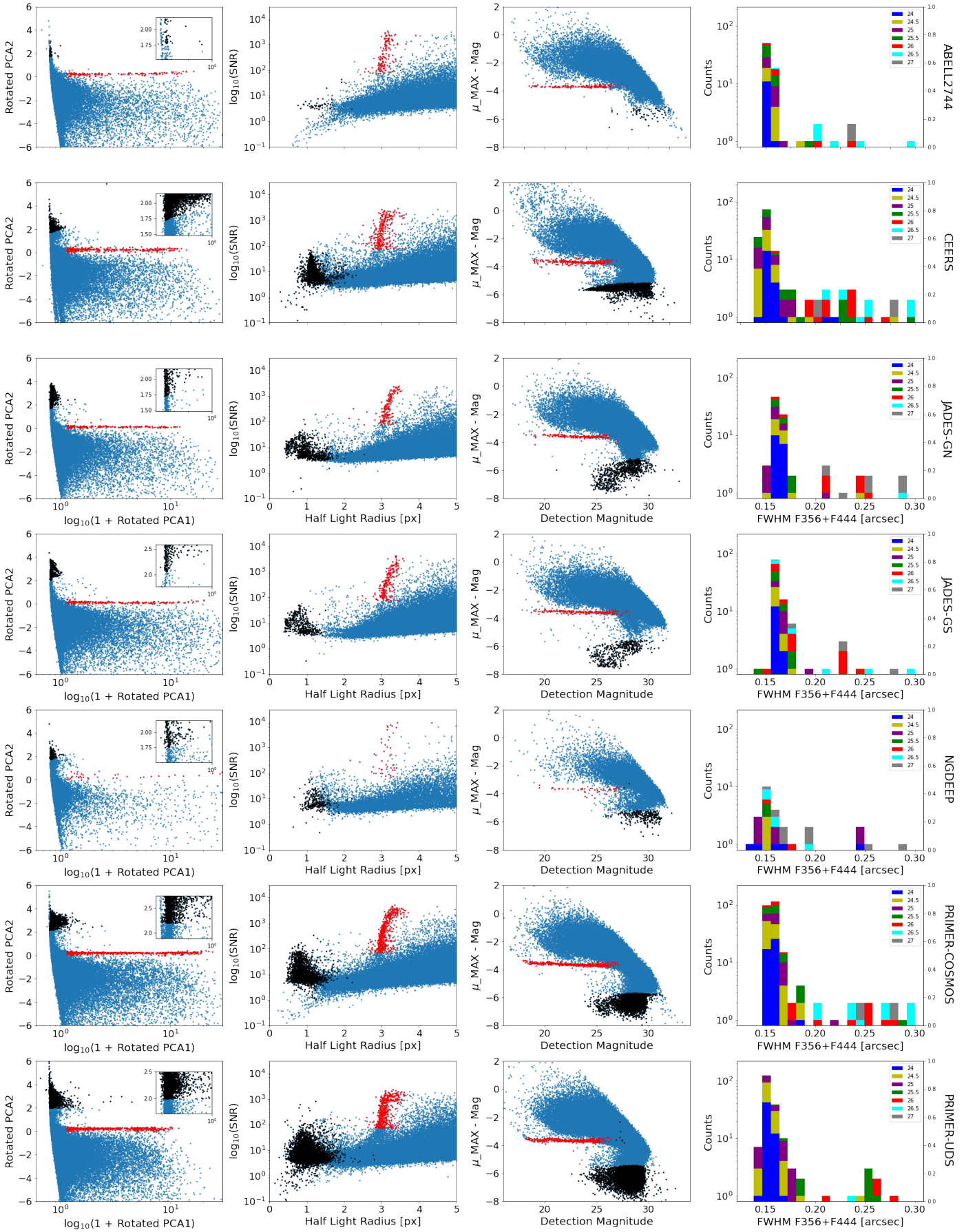


**Fig. C.1:** Star/galaxy separation and flagging of spurious sources. From left to right: as obtained in the PCA plane described in Sect. 3.5, projected on the hlr vs. SNR plane, projected on the  $\mu_{\text{MAX}}$ -MAG vs. MAG plane. The last column shows the values of the FWHM in the detection F356W+F444W stack, for the sources identified as point-source.

## **Appendix D: Depth of mosaics**

The histograms in Fig. D.1 show the  $5\sigma$  limiting magnitudes of the mosaics in apertures of  $0.2''$ , computed from the re-scaled RMS maps, as described in Sect. 3.2.

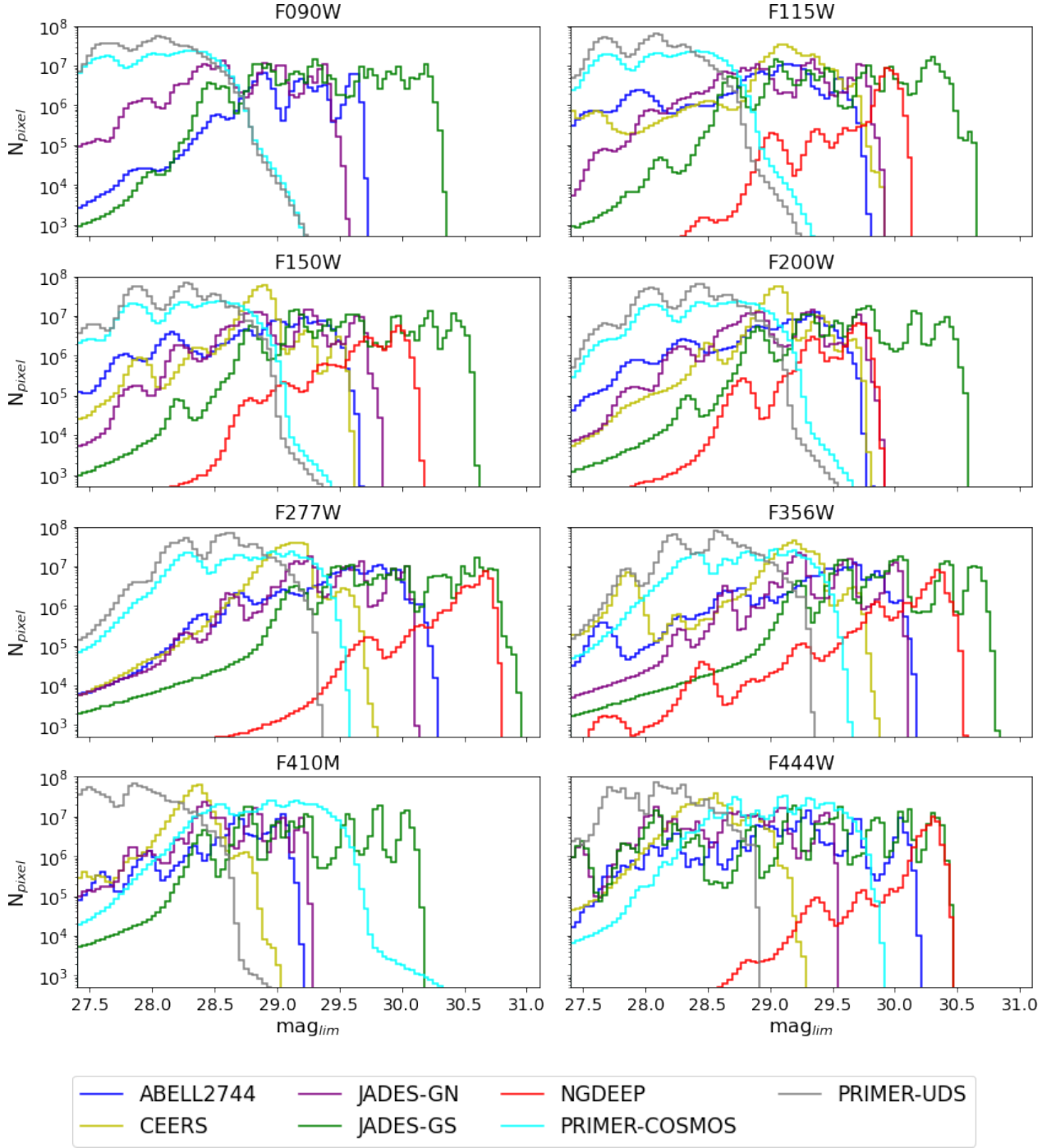


**Fig. D.1:** Histograms of the pixel distributions of limiting magnitudes (total at  $5\sigma$  in  $0.2''$  diameter apertures), computed as described in Sect. 3.2, for all bands and fields.

## Appendix E: Comparisons with other photometric catalogs

Fig. E.1 to E.6 show how the photometry obtained in this work compares to that from other available catalogs. For each field we consider recent NIRCcam-based catalogs and archival *HST* based data, from CANDELS or ASTRODEEP. For the latter, we used the *Ks* and IRAC CH1-2 bands as proxys for the F200W, F356W and F444W *JWST* bands, applying the following color corrections, based on Bruzual & Charlot (2003) theoretical templates:  $Ks = F200W - 0.06$ ,  $IRAC1 = F356W + 0.02$ ,  $IRAC2 = F444W - 0.01$ .

Each panel of the plots shows the comparison for one color, with the relative difference  $\Delta c/c$  (i.e. color measured in this work minus color in the reference work, divided by color in the archival work) as a function the magnitude of the second band in this work (e.g., F444W magnitude if the color is F356W-F444W). The blue line is the median of the distribution. We consider sources with  $\text{SNR} > 5$  and  $\text{flag} < 200$ . See Sect.4 for more details.

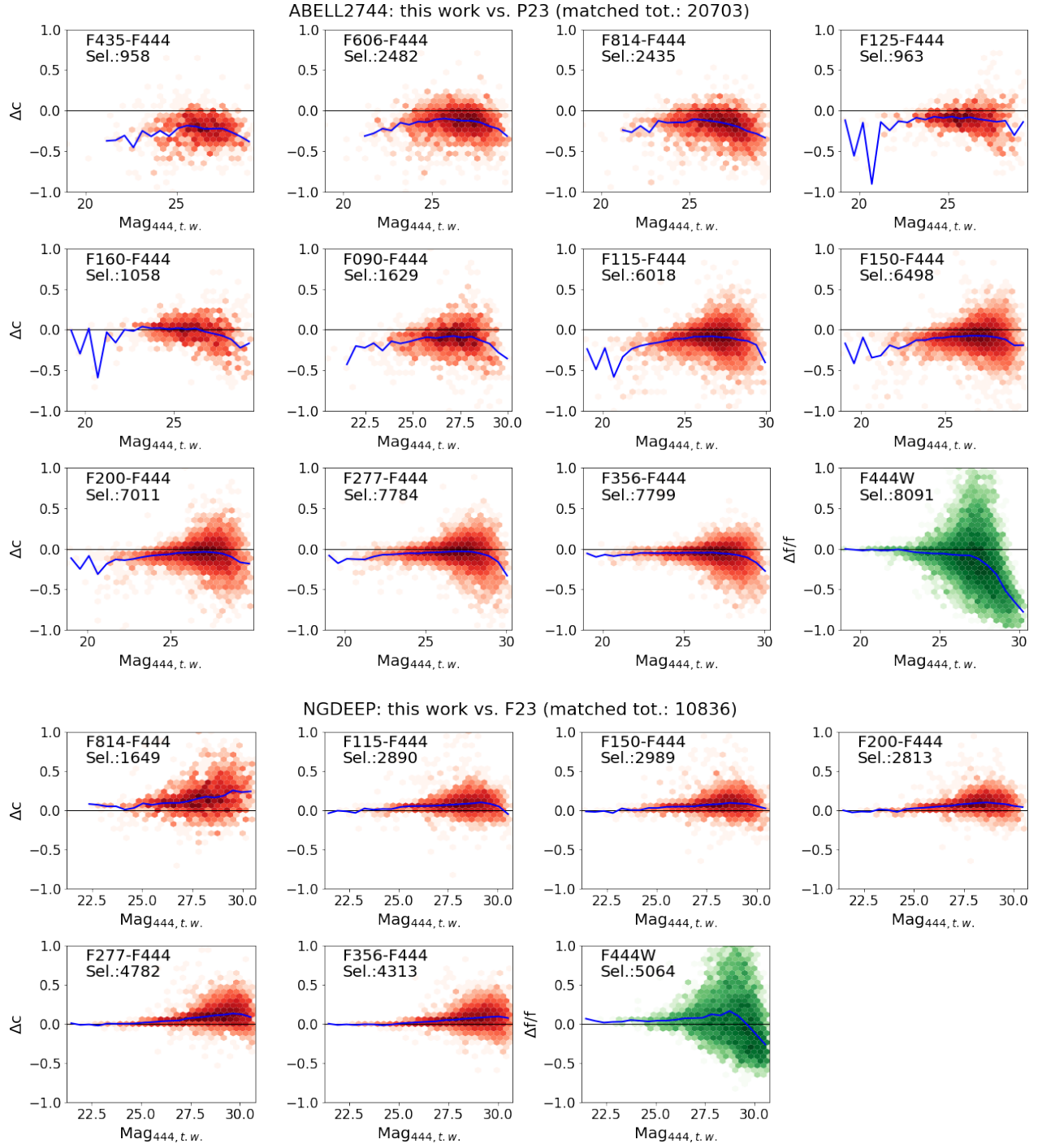


**Fig. E.1:** Comparison of colors measured in this work and archival catalogs. Shown are relative errors  $\Delta c$  i.e. the colors measured in this work minus those in the reference catalogs), vs. the second band magnitude in this work catalog (e.g. F444W for the F356-F444W color). Top to bottom: ABELL2744 vs. P23 and NGDEEP vs. Finkelstein's catalog (priv. comm.). The number of cross-matched sources after excluding those with SNR  $< 5$  in any of the two catalogs or flag  $\geq 200$  in this work is also given in each panel; the blue line is the median of the distribution.



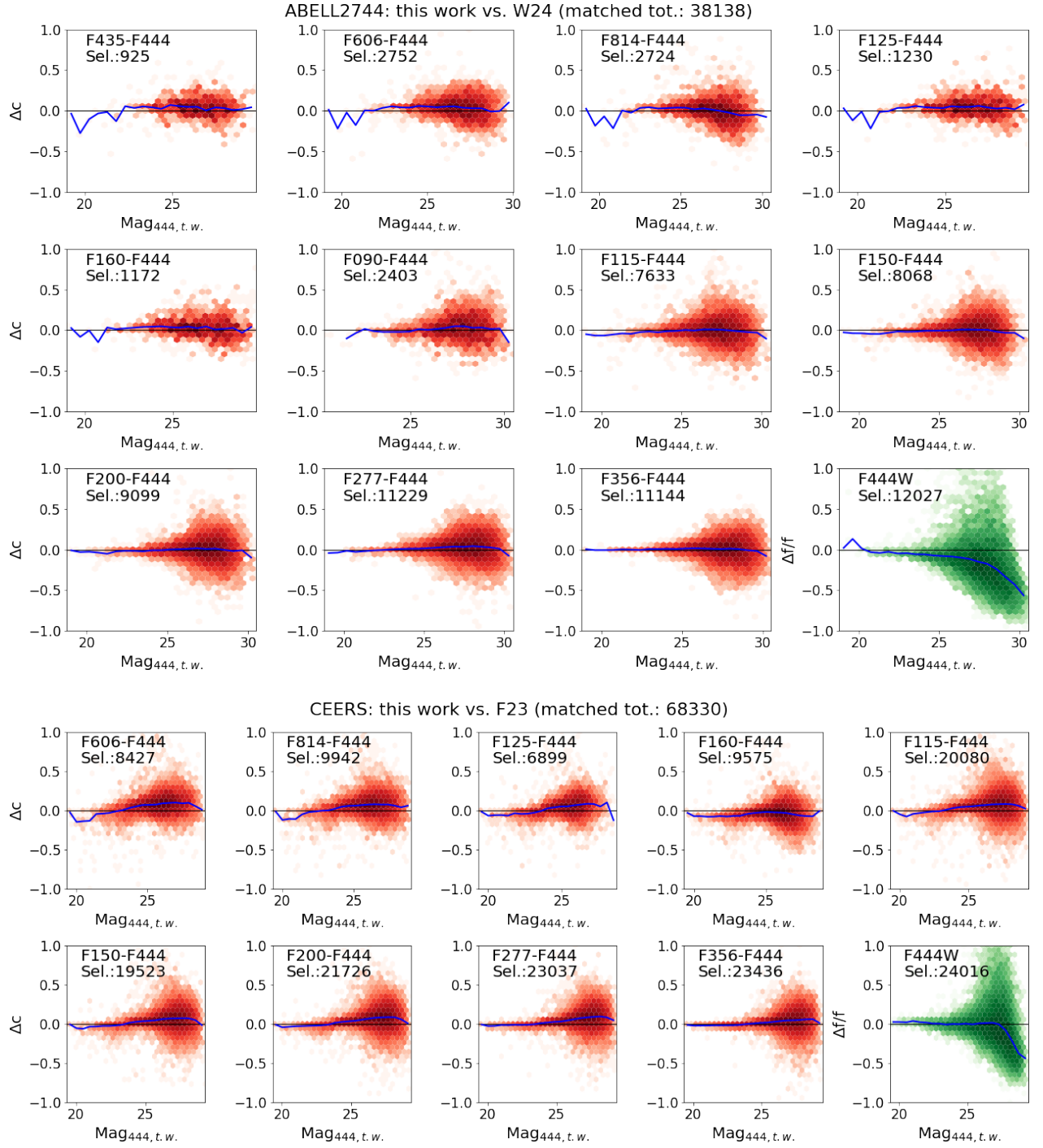


**Fig. E.2:** Same as Fig. E.1, for (top to bottom) ABELL2744 vs. Weaver et al. (2024) and CEERS vs. Finkelstein et al. (2023a).

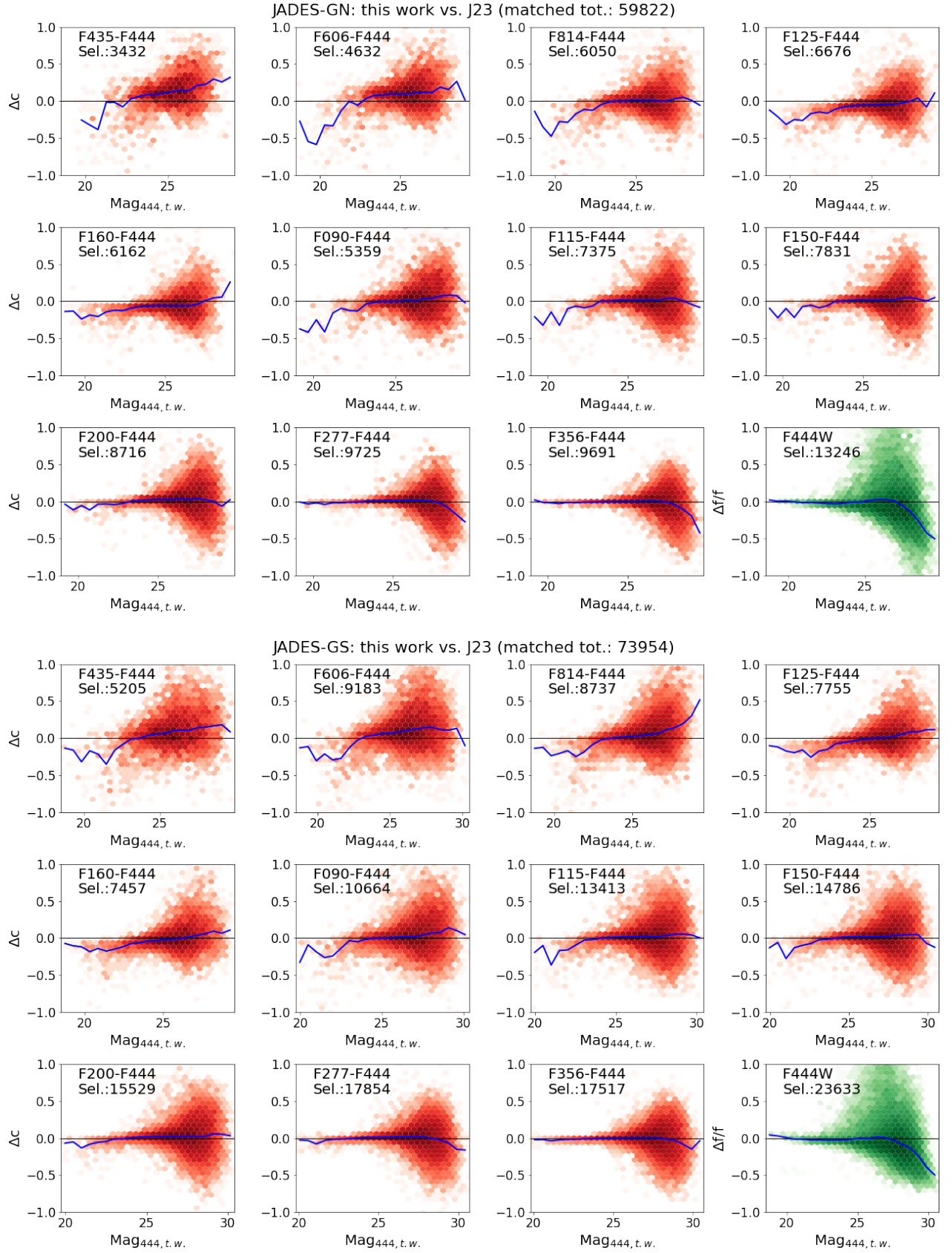
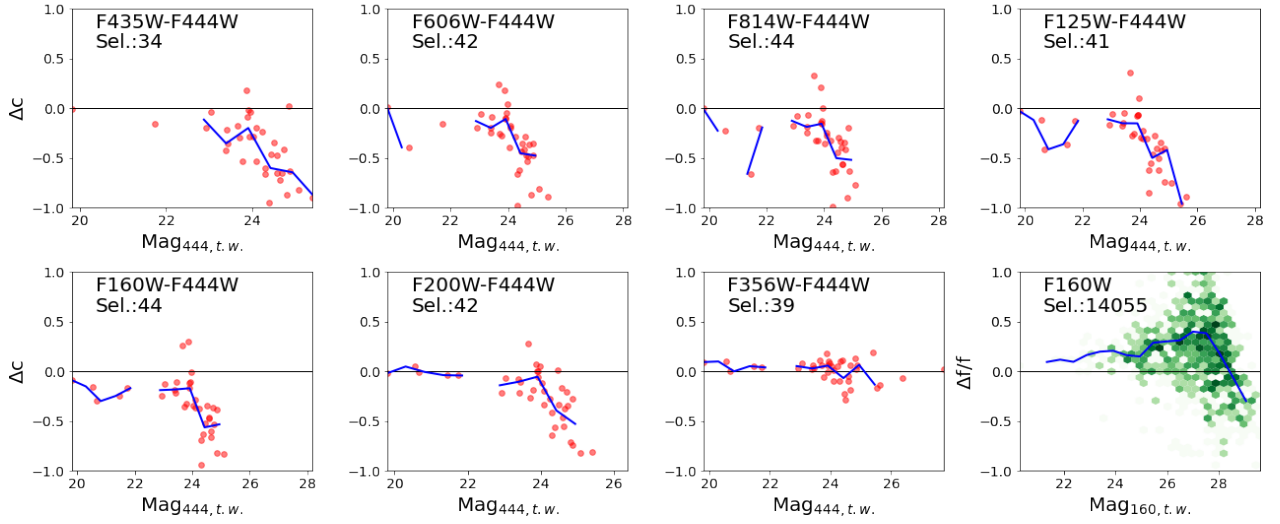


**Fig. E.3:** Same as Fig. E.1, for JADES-GN and JADES-GS vs. the JADES team catalogs (Rieke et al. 2023).

ABELL2744: this work vs. ASTRODEEP-FF (matched tot.: 2560)



PRIMER-UDS: this work vs. CANDELS (matched tot.: 28222)

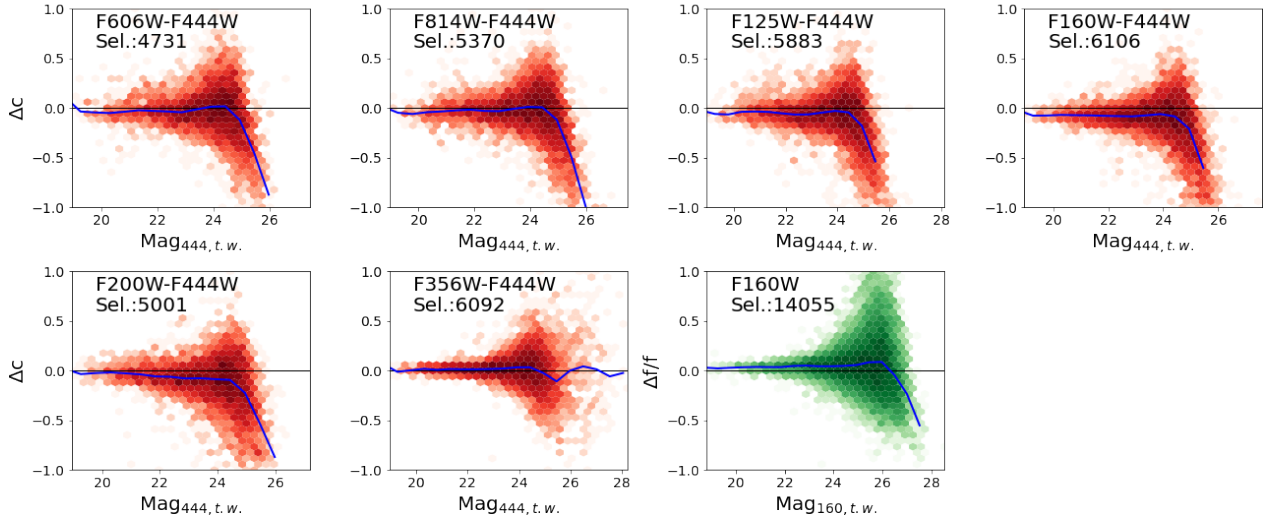


**Fig. E.4:** Same as Fig. E.1, for ABELL2744 vs. Merlin et al. (2016b) showing individual points rather than a density *hexbin* plot because of the small number of cross-matched sources, and PRIMER-COSMOS vs. Nayyeri et al. (2017). The *HST* colors are transformed into *JWST* colors by means of the corrections described in Appendix E.

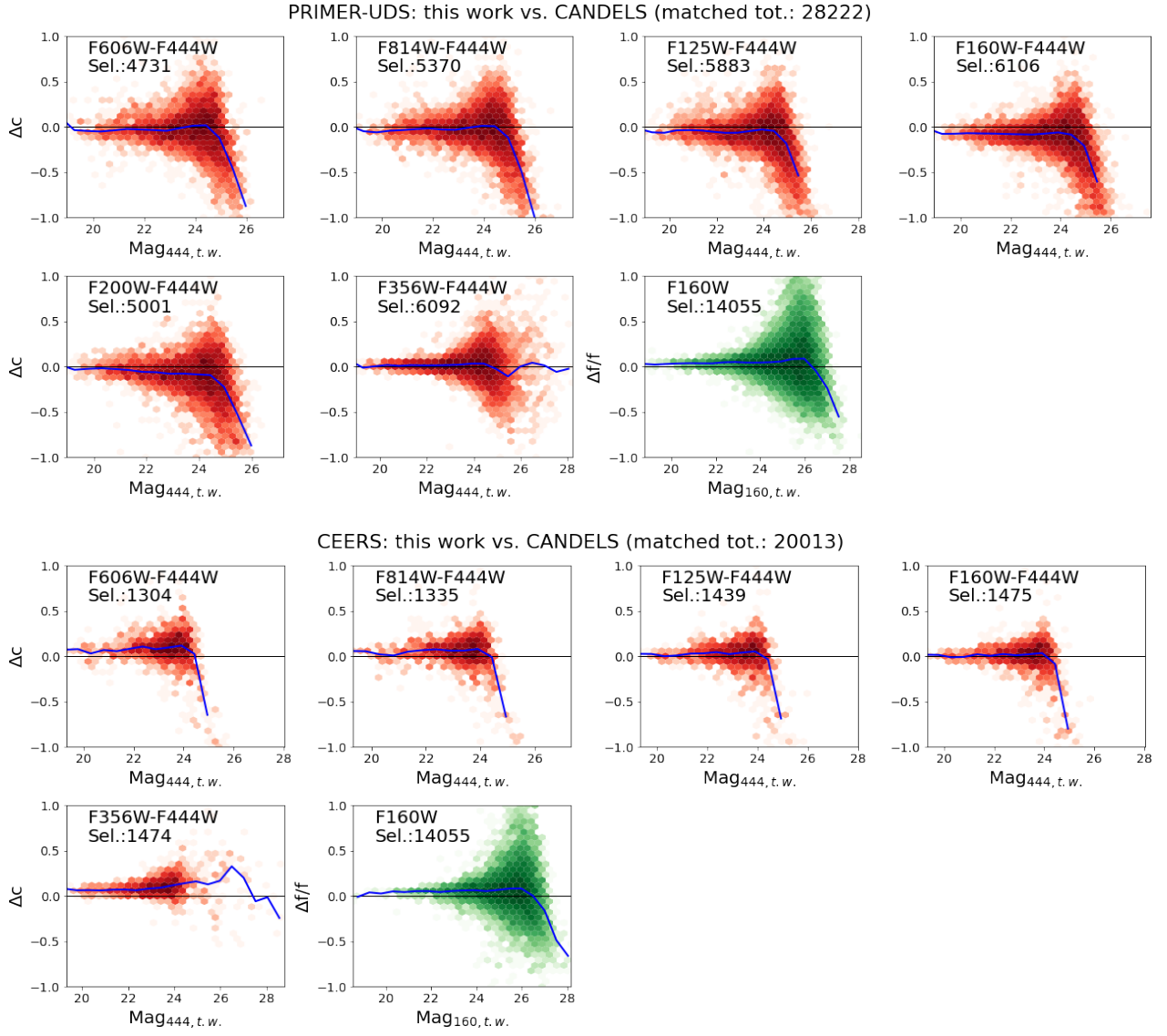


**Fig. E.5:** Same as Fig. E.1, for PRIMER-UDS vs. Galametz et al. (2013), and CEERS vs. Stefanon et al. (2017).



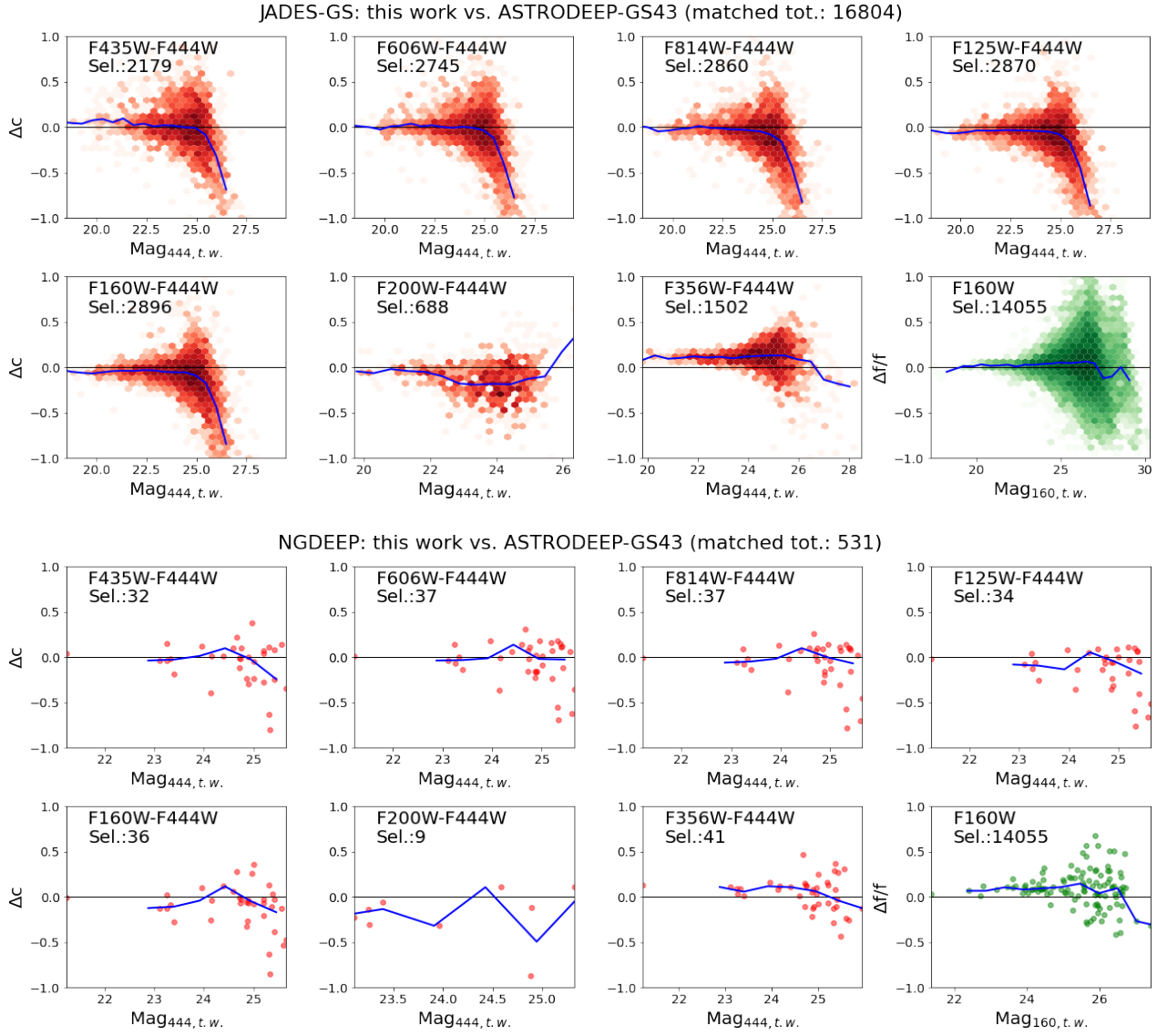


**Fig. E.6:** Same as Fig. E.1, JADES-GS vs. Merlin et al. (2021) and NGDEEP vs. Merlin et al. (2021), the latter showing individual points rather than a density *hexbin* plot because of the small number of cross-matched sources. The *HST* colors are transformed into *JWST* colors by means of the corrections described in Appendix E.

## Appendix F: Photometric redshifts validation

In Figs. F.1 we show the comparison between the spectroscopic and photometric redshifts, the latter computed as the median of the three runs with (i) `zphot`, (ii) EAzy with `eazy_v1.3`, and (iii) EAzy with Larson et al. (2023b) FSPS Set 1 + Set 4 templates, as described in Sect. 5. Table F.1 summarizes the statistics for all the four runs.

**Table F.1:** Compared statistics for photometric vs. spectroscopic redshifts. The listed values are: number  $N$  of matched sources (the number can vary due to failings in the fitting procedures of the different codes); mean, standard deviation, median and NMAD of the quantity  $|z_{phot} - z_{spec}|/(1 + z_{spec})$ , all multiplied by 100 to make the differences clearer; and percentage of outliers  $f_{outliers}$  as described in Sect. 5, for each run using a different software and/or templates, and for each field.

	N	100×mean	100×stdev	100×median	100×NMAD	$\eta$
ABELL2744						
ZPHOT	1209	0.72	4.18	0.57	3.28	9.35
EAzY v1.3	1208	-0.77	4.24	-0.37	3.25	12.83
EAzY Larson Lya	1192	0.04	4.53	-0.14	3.21	14.18
EAzY Larson LyaRed	1192	-0.12	4.58	-0.19	3.26	14.77
CEERS						
ZPHOT	3081	1.19	4.63	0.92	3.69	7.95
EAzY v1.3	3077	0.37	4.51	0.44	3.59	7.47
EAzY Larson Lya	3076	-0.41	4.96	-0.29	4.05	8.78
EAzY Larson LyaRed	3076	-0.41	4.96	-0.32	4.09	8.91
JADES-GN						
ZPHOT	1827	0.81	4.23	0.76	3.50	6.79
EAzY v1.3	1825	-0.22	4.31	0.04	3.01	8.82
EAzY Larson Lya	1820	-0.74	4.10	-0.53	2.91	8.52
EAzY Larson LyaRed	1820	-0.78	4.11	-0.54	2.97	8.74
JADES-GS						
ZPHOT	2016	0.43	4.00	0.34	3.02	5.80
EAzY v1.3	2014	-0.56	4.05	-0.32	2.90	10.03
EAzY Larson Lya	2012	-0.74	3.80	-0.47	2.84	9.94
EAzY Larson LyaRed	2012	-0.84	3.83	-0.54	2.87	10.24
NGDEEP						
ZPHOT	128	1.46	4.08	0.92	3.10	10.16
EAzY v1.3	128	-0.10	4.26	0.21	3.62	9.38
EAzY Larson Lya	128	-0.29	4.16	-0.14	3.76	15.62
EAzY Larson LyaRed	128	-0.29	4.18	-0.10	3.80	16.41
PRIMER-COSMOS						
ZPHOT	4298	1.37	4.60	1.35	4.16	7.00
EAzY v1.3	4293	-0.09	4.56	0.06	3.64	7.43
EAzY Larson Lya	4284	-0.68	4.69	-0.41	3.90	9.03
EAzY Larson LyaRed	4284	-0.68	4.70	-0.41	3.92	9.15
PRIMER-UDS						
ZPHOT	3710	1.03	4.50	0.96	3.80	5.80
EAzY v1.3	3708	-0.06	4.54	0.09	3.65	5.18
EAzY Larson Lya	3702	-0.65	4.85	-0.43	3.85	7.43
EAzY Larson LyaRed	3702	-0.65	4.85	-0.46	3.87	7.59

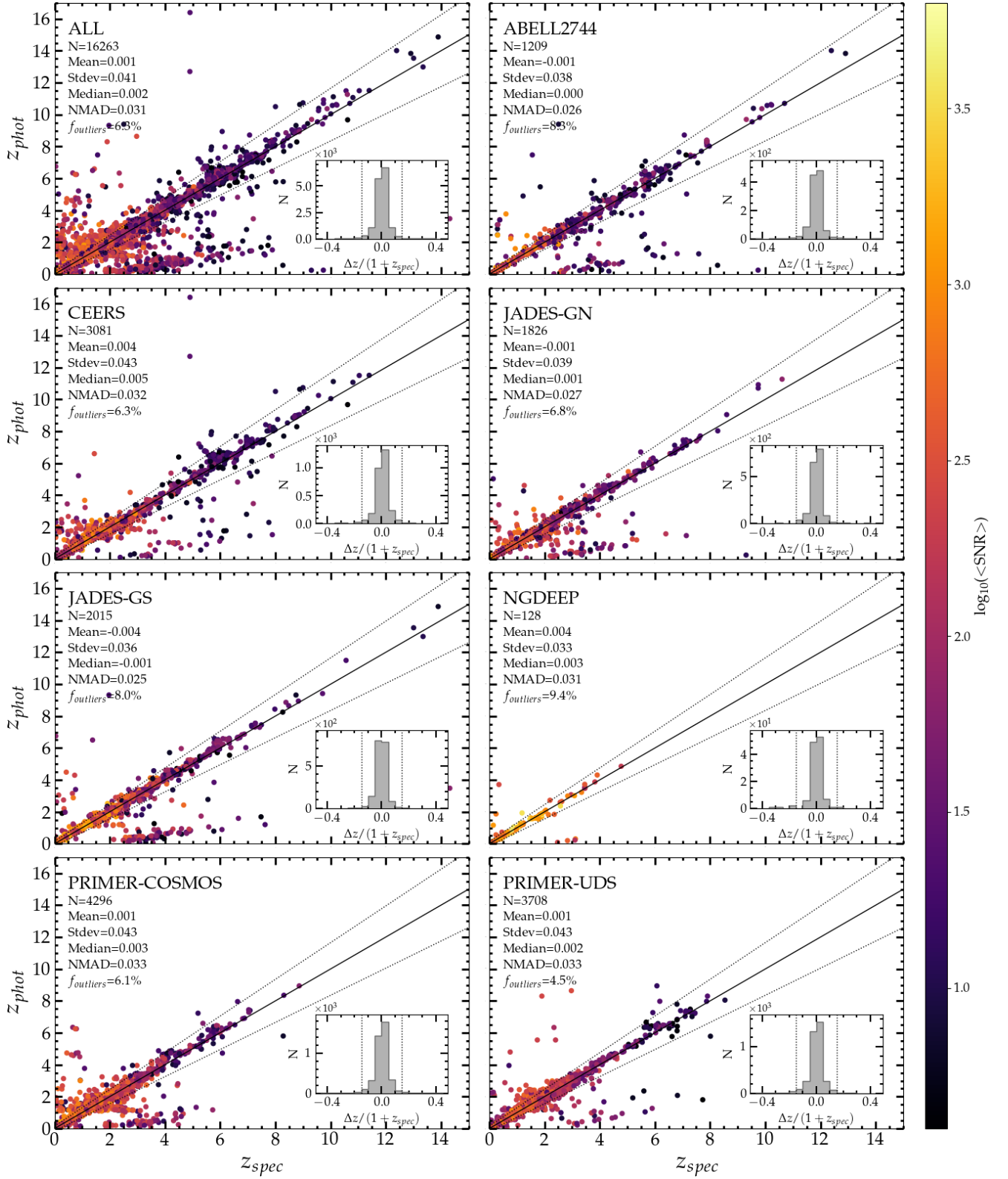


**Fig. F.1:** Accuracy of photometric redshifts (median of the three runs described in Sect. 5) on spectroscopic samples, for all fields together (top left panel), and separately for each field. In each panel,  $N$  is the number of sources;  $f_{\text{outliers}}$  is the percentage of sources with  $|z_{\text{phot}} - z_{\text{spec}}|/(1 + z_{\text{spec}}) > 0.15$ ; the other statistics are computed on non-outliers, with  $\text{NMAD} = 1.48 \times \text{median}[|z_{\text{phot}} - z_{\text{spec}}|/(1 + z_{\text{spec}})]$ . Color coding is  $\log_{10}(\langle \text{SNR} \rangle) = (\text{SNR}_{\text{F444W}} + \text{SNR}_{\text{F356W}} + \text{SNR}_{\text{F277W}} + \text{SNR}_{\text{F200W}})/4$ .